Contents lists available at ScienceDirect

Arabian Journal of Chemistry

journal homepage: www.ksu.edu.sa

# Insights on Z-scheme interfacial charge transfer of $TiO_2$-NRAs/BiOI-NFs/Au-NPs nanoheterostructures and unveiling enhanced photoelectrochemical performances

Zhufeng Shao [a,*], Yonglong Zhang [a,c], Xiujuan Yang [a], Guoyang Yu [c], Yunfei Song [c], Min Zhong [b], Xiaoming Xiu [a,*]

[a] *College of physical science and technology, Bohai University, Jinzhou, Liaoning 121000, China*
[b] *College of chemistry and materials engineering, Bohai University, Jinzhou, Liaoning 121000, China*
[c] *National Key Laboratory of Shock Wave and Detonation Physics, Institute of Fluid Physics, China Academy Of Engineering Physics, Mianyang, China*

ARTICLE INFO

*Keywords:*
$TiO_2$-NRs/BiOI-NFs/Au-NPs ternary nanoheterostructure
oxygen vacancies defect states
Z-scheme charge transfer
photoelectrochemical degradation

ABSTRACT

We synthesized $TiO_2$-NRAs/BiOI-NFs/Au-NPs ternary Z-scheme nanoheterostructure using an accessible preparation method. The ternary nanoheterostructure

exhibited enhanced photoelectrochemical (PEC) performance compared to other binary nanoheterostructure. The improved performance was attributed to the synergistic effect between enhanced charge separation and improved injection efficiency. An interfacial charge migration mechanism involving plasmon-induced hot electron injection and transition with oxygen vacancies defects was proposed. The triple nanohybrids showed a higher photodegradation rate for methyl orange (MO). Based on the scheme, the $TiO_2$-NRAs/BiOI-NFs/Au-NPs ternary nanohybrids exhibited a photodegradation rate of 96.6% toward degradation of MO irradiated by UV-visible light, 1.47 and 1.19 fold that of BiOI-NFs/Au-NPs and $TiO_2$-NRAs/BiOI-NFs, respectively. Furthermore, the $TiO_2$-NRAs/BiOI-NFs/Au-NPs ternary nanoheterojunction exhibits the best photodegradation performance under near-infrared light irradiation, with a photodegradation rate 4.3 times and 1.2 times that of the binary $TiO_2$-NRAs/BiOI-NFs and BiOI-NFs/Au-NPs nanoheterojunction composites, respectively. These findings provide insights into interfacial charge transfer in $TiO_2$-NRAs/BiOI-NFs/Au-NPs nanoheterostructures and demonstrate their enhanced PEC performances, inspiring the design of high-efficiency and non-toxic Z-scheme heterostructures for various applications.

## 1. Introduction

Environmental pollution and the prevalence of various diseases have posed significant threats to human health over an extended period. In the early 1880s, Fujishima and Honda's groundbreaking work (Fujishima and Honda, 1972) on semiconductor-based photoelectrochemical (PEC) energy conversion paved the way for the development of photodegradation technology as a promising and eco-friendly method for efficient and cost-effective removal of organic pollutants. (Zhao et al., 2024) Generally, an integrated PEC process involving photo-triggered semiconductor materials comprises five main steps: (i) photo-excited light absorption; (ii) generation of electron - hole ($e^-$ - $h^+$) pairs; (iii) transfer and recombination of charge carriers; (iv) adsorption-desorption of target molecules; and (v) redox reactions on the semiconductor material's surface. The overall PEC activity is determined by these five processes collectively, with the effective charge transfer (CT) and rapid carrier injection playing pivotal roles. (Zhu et al., 2022) To enhance the PEC performance in photodegradation, researchers have explored various methods. Among these strategies, heterostructure nano-devices have garnered significant attention, benefiting from their ability to narrow the band-gap, improve carrier separation efficiency, accelerate CT rates, enhance reduction and oxidation potentials, and increase the number of redox active sites. (Wang et al., 2022) These heterostructure designs primarily include type-II heterojunctions, Schottky-like heterojunctions, and Z-scheme heterostructures. (Li et al., 2023)

$TiO_2$ has been widely recognized as an excellent n-type material for PEC applications in decomposition due to its non-toxicity, abundance,

---

* Corresponding authors.
*E-mail addresses:* jinhaiyuan@126.com (Z. Shao), xiuxiaomingdl@126.com (X. Xiu).

https://doi.org/10.1016/j.arabjc.2024.105765
Received 22 December 2023; Accepted 29 March 2024

stable physicochemical properties, and resistance to photocorrosion. (Hoseini and Yarmand, 2023) The hydrothermal growth of self-grown $TiO_2$ nanorod arrays ($TiO_2$-NRAs) on a transparent conductive oxide substrate has provided a direct electron transport pathway along the axial direction and increased the specific surface area, thereby reducing carrier recombination rates, enhancing charge separation, and facilitating the rapid release of carriers into the electrolyte. (Wang et al., 2023) However, despite the favorable characteristics of $TiO_2$-NRs, they still exhibit certain drawbacks for efficient PEC activity, including limited light absorption in the solar spectrum, high $e^-$ - $h^+$ pairs recombination rates, and low quantum yield. (Sun et al., 2023) To overcome these challenges, the construction of $TiO_2$-NRs-based heterojunction nanocomposites has been regarded as one of the most effective strategies. This approach harnesses the powerful built-in electric fields (BEF) and intrinsic defects, such as oxygen vacancies ($V_o$) defects. (Shao et al., 2022) Notably, Xu's team reported the hydrothermal synthesis of a $BiOCl/TiO_2$ type-II nanoheterojunction for ultraviolet photodetection, achieving remarkable detectivity. This success was attributed to the strong BEF formed at the heterojunction interface and the efficient carrier transmission characteristics of the $TiO_2$ film. (Zhang et al., 2022) Furthermore, Chen and co-workers (Chen et al., 2022) fabricated a $V_o$-enriched anatase/rutile $TiO_2$ heterostructure, which exhibited expanded visible light absorption and enhanced charge carrier separation.

Bismuth oxyhalide (BiOX, X = Cl, Br, I) materials have gained significant attention in recent years due to their excellent PEC properties. Among them, bismuth oxyiodide (BiOI) stands out as a promising material for constructing photodegradation. BiOI has a narrow band gap (1.6 eV - 1.9 eV), making it favorable for visible light absorption. (Hu et al., 2022) Additionally, the lamellar nanoflake structure of BiOI (BiOI-NFs) not only facilitates the formation of an internal electric field between the Bi-O layers, promoting efficient separation of photoexcited electron-hole pairs, but also provides a high specific surface area that increases the number of active sites available for redox reactions on the BiOI-NFs surface, thereby enhancing its overall PEC performance in photocatalysis applications. (Shan et al., 2024) However, separated BiOI often experiences rapid recombination of photoexcited charge carriers and exhibits weak redox abilities. (Xia et al., 2022) To address these limitations, researchers have focused on enhancing the quantum efficiency and redox capacity of BiOI by constructing heterostructures with other semiconductors. For instance, Chen et al. (Chen et al., 2023) reported the fabrication of $BiOI/TiO_2$ p-n heterojunctions via hydrothermal synthesis, which effectively accelerated the separation and transfer of photoinduced carriers and broadened the light absorption range. Nevertheless, the photocatalytic activity of these heterojunctions remained limited due to the involvement of fewer active sites in the reaction. Alternatively, it has been demonstrated that constructing Schottky-like heterojunctions by decorating BiOI with plasmonic metals can lead to enhanced PEC performance. Qiao et al. (Qiao et al., 2023) showed that the synergistic effects of localized surface plasmon resonance (LSPR) hot electron injection and charge separation improved the PEC efficiency of Au/BiOI nanocomplexes, primarily due to the increased active sites on the BiOI surface. Moreover, Au nanoparticles (NPs) have been found to induce the generation of $V_o$ defects in adjacent semiconductors through the LSPR effect. (Cui et al., 2022) This introduction of $V_o$ defects optimizes the active sites at the solid-liquid interface, elevates the redox potential of the energy band, promotes the formation of reactive oxygen species (ROS), and facilitates the separation of photoexcited carriers. (Jin et al., 2023) Similarly, Qu et al. (Qu et al., 2022) introduced abundant $V_o$ defects in BiOI via a hydrolysis process, extending the absorption region to a wider wavelength range and facilitating the migration of photoexcited electrons to adsorbed molecules on the BiOI surface.

Combining the advantages of p-n heterojunction and Schottky-like heterojunctions in aspect of CT, the Z-scheme heterostructure nanosystem has drawn great interest in PEC applications, which not only possesses high CT efficiency but also retain superior redox ability due to its Z-type carrier migration route. Especially, the formation of Z-scheme heterojunction can greatly improve the PEC activity of BiOI, due to the facilitation in the separation and transport of photogenerated $e^-$ - $h^+$ pairs. Thus, evidently improved PEC performance for meeting the need of strong photodegradation activity and sensitive bioanalysis could be obtained. Encouraged by these finding, $Ag/BiOI/TiO_2$ and $Au/BiOI/TiO_2$ ternary Z-scheme heterojunction nanohybrids have been separately applied for the fabrication of sensitive PEC aptasensing for detecting chloramphenicol and photocatalytic nitrogen fixation. (Wu et al., 2022; Xin et al., 2023) It is worth emphasizing that, compared to other ternary nanocomposites involving BiOI, we are inclined to believe that the construction of novel $TiO_2$-NRAs/BiOI-NFs/Au-NPs integrates the advantages of the lamellar BiOI-NFs structure could exhibit promising PEC performance owing to the synergistic effects of the Z-scheme CT mechanism, a high surface area, improved redox capabilities, and plasmonic effects from the Au NPs which can also induce intrinsic $V_o$ defects.

In summized, we constructed adventurous $TiO_2$-NRAs/BiOI-NFs/Au-NPs ternary nanoheterojunctions by a facile straightforward electrodepositing approach as expected, and the characterizations of optical and chemical components for as-prepared specimens were examined by UV-visible diffuse reflectance spectrophotometry (UV-vis DRS) spectra, X-ray diffraction (XRD), Raman spectra, and X-ray photoelectron spectroscopy (XPS). Additionally, a seires of PEC experimental results exhibited that the improved PEC performances of $TiO_2$-NRAs/BiOI-NFs/Au-NPs ternary nanoheterojunctions compared with that of $TiO_2$-NRAs/BiOI-NFs and BiOI-NFs/Au-NPs binary nanoheterostructures, mainly ascribing to the photoinduced Z-scheme CT process, which verified by transient photoluminescence (PL) spectra combined with energy level analysis. Thanks to these advantages of the $TiO_2$-NRAs/BiOI-NFs/Au-NPs ternary Z-scheme nanoheterojunctions, including the more effective CT rate and the stronger redox capability, which resulted in an enhanced PEC activities for photodegradation. To the best of our knowledge, many works reported that the Z-scheme heterostructured nanohybrids possessed a higher PEC performance than that of the component. Little work focused on the Z-scheme CT mechanism and efficiency probed by transient-PL spectrum approach. Yet, our results have provided further direct experimental evidence in favor of photoinduced interfacial Z-scheme CT dynamics for $TiO_2$-NRAs/BiOI-NFs/Au-NPs ternary nanocomposites, which are approved by the nanosecond time-resolved transient PL spectra (NTRT-PL). We greatly hope that this research would inspire interests in the design and construct a well-defined Z-scheme heterostructure system with a verified, reliable CT mechanism for pushing forward the practical application of photodegradation.

## 2. Experimental Section

### 2.1. Preparation of $TiO_2$-NRAs substrates via hydrothermal systhesis

All reagents and solvents were procured from commercial sources and used without any further purification. Prior to the reaction, the fluorine-doped tin oxide (FTO) substrate measuring 1 cm × 1.5 cm was thoroughly cleaned using acetone, ethanol, and deionized (DI) water. The growth of $TiO_2$-NRAs was achieved directly on the FTO substrate via a hydrothermal method. To initiate the process, 30 ml of DI water and 30 ml of HCl were combined, mixed, and stirred for a duration of 10 minutes. Subsequently, 1 ml of butyl titanate was added to the solution, followed by an additional 15 minutes of stirring. The resulting solution was then transferred into a reactor, with the clean FTO substrate positioned vertically on the inner wall of the reactor. The reaction was allowed to proceed for 6 h at a temperature of 150°C, after which the samples were rinsed with DI water. Finally, the samples were subjected to calcination in air at 450°C for a duration of 90 minutes.

### 2.2. Fabrication of binary $TiO_2$-NRAs/BiOI-NFs nanoheterojunctions, and pristine BiOI-NFs/FTO films

The fabrication of BiOI-NFs was accomplished using a conventional electrodeposition method. Initially, 3.32 g of potassium iodide (KI) was dissolved in 50 ml of deionized water to prepare a 0.4 M aqueous solution of KI. Subsequently, 0.97 g of bismuth nitrate pentahydrate ($Bi(NO_3)_3 \cdot 5H_2O$) was dissolved in the aforementioned KI solution, and the pH value was adjusted to 1.7. This KI solution containing $Bi(NO_3)_3 \cdot 5H_2O$ was designated as solution A. On the other hand, a mixture of 20 ml of anhydrous ethanol and 0.50 g of p-benzoquinone was prepared and labeled as solution B. The solutions A and B were combined and vigorously stirred for a duration of 30 minutes to facilitate electrodeposition. The electrodeposition process was carried out in a three-electrode cell, employing prepared $TiO_2$-NRAs and FTO substrates as the working electrode, Ag/AgCl as the reference electrode, and platinum (Pt) wire as the counter electrode. Electrodeposition was performed at -0.1 V vs. Ag/AgCl for 5 minutes at room temperature. As a result, a uniform orange film consisting of BiOI-NFs was formed on both the $TiO_2$-NRAs and FTO substrates. Consequently, $TiO_2$-NRAs/BiOI-NFs binary nanoheterojunctions and pure BiOI-NFs/FTO films were successfully obtained, respectively.

### 2.3. Synthesis of ternary $TiO_2$-NRAs/BiOI-NFs/Au-NPs nanoheterostructures, and binary BiOI-NFs/Au-NPs Schottky-like heterojunctions nanohybrids

To begin with, ultra-thin Au films were deposited onto the substrates of $TiO_2$-NRAs/BiOI-NFs and single BiOI-NFs. This deposition process involved fixing the sputtering time to 30 s, resulting in a film thickness of less than 10 nm. The deposition took place in a vacuum chamber using an ion sputtering system (Hitachi, E-3010), with a sputtering current of 10 mA. The chamber was maintained at a pressure of $4 \times 10^{-2}$ Pa, and the sputtering power of the Au target was set to 30 W. Subsequently, the Au films on the surface of the prepared samples underwent rapid annealing at a temperature of 200°C for a duration of 30 minutes. This annealing process facilitated the transformation of the Au film into Au NPs. The precise preparation of the specimens, namely $TiO_2$-NRAs/BiOI-NFs/Au-NPs and BiOI-NFs/Au-NPs, was crucial to achieve well-defined structures with distinct Au NPs, preventing their aggregation. This controlled preparation method played a vital role in obtaining visually appealing structures with properly dispersed Au NPs on the surfaces of both $TiO_2$-NRAs/BiOI-NFs and BiOI-NFs substrates. This, in turn, contributed to the effective suppression of Au NP aggregation, as demonstrated in the subsequent morphological characterization.

It is highlighted that the annealing process was performed as the same conditions for samples of $TiO_2$-NRAs/BiOI-NFs, BiOI-NFs/Au-NPs and single BiOI films, which of them acting as the references for characterization of optical and PEC performances, and the incorporation procedures of $TiO_2$-NRAs/BiOI-NFs/Au-NPs, $TiO_2$-NRAs/BiOI-NFs, BiOI-NFs/Au-NPs, and single BiOI films in detail as presented in scheme 1.

### 2.4. Characterization

The morphologies of the heterostructure nanocomposites were examined using scanning electron microscopy (SEM, Hitachi S4200) at an accelerating voltage of 15.0 kV, providing both top-view and cross-sectional images. UV-vis DRS was conducted at room temperature in air, utilizing a UV-vis spectrophotometer (UV-1800, Shimadzu). Transmission electron microscopy (TEM) analysis was carried out using a transmission electron microscope (JEOL JEM-2100) operating at 200 kV. The phase purity and crystal structure of the prepared samples were characterized using an XRD (Shimadzu XRD-600) with Cu Kα radiation ($\lambda = 15.418$ nm). The XRD scans were performed in the 2θ range of $20^o$ to $80^o$ at a scanning rate of $0.02^o$/s. XPS (ESCALAB 250, Thermo Fisher Scientific Ltd.) was employed to examine the oxidation states of titanium (Ti) and bismuth (Bi) elements on the surface of as-obtained specimens. The XPS measurements utilized an Al anode as the X-ray source, emitting Kα (1486.6 eV) radiation at 150 W. The XPS energy scale was calibrated using the Ag $3d_{5/2}$ line on clean silver, aligning it with the Fermi level ($E_F$) set at 368.3 eV. The energy axis of the XPS spectra was adjusted due to specimen charging during X-ray irradiation, and the C1s binding energy (BE) line at 285.0 eV was used as a reference for the charging effect. Crystal structure and chemical bonding states of the prepared nanocomposites were investigated using Micro-Raman spectroscopy (Horiba JY-HR800) equipped with a confocal microscope. The Raman measurements employed an $Ar^+$ laser operating at 532 nm with an excitation power of 6 mW at room temperature. The specific surface areas of the obtained specimens were determined using the Brunauer-Emmett-Teller (BET) method, based on $N_2$ adsorption and desorption isotherms collected on an ASAP 2020 instrument. The

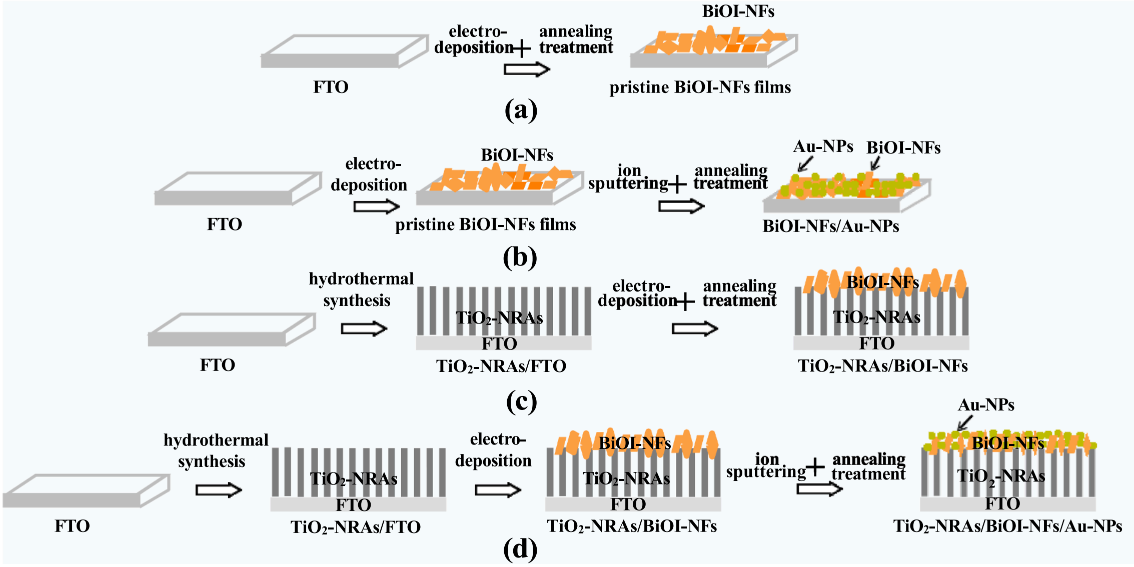

**Scheme 1.** Synthetic procedures for preparation of pristine BiOI films (a), BiOI-NFs/Au-NPs (b), $TiO_2$-NRAs/BiOI-NFs (c), and (d) $TiO_2$-NRAs/BiOI-NFs/Au-NPs ternary heterostructures nanohybrids, respectively.

electrochemical double-layer capacitance of each synthesized material was measured using cyclic voltammetry (CV) in the non-faradaic region, ranging from 0.128 V to 0.228 V versus the reversible hydrogen electrode (RHE), with different scan rates (20 mV/s, 40 mV/s, 60 mV/s, 80 mV/s, and 100 mV/s) to estimate the effective electrode surface area.

A Ti:sapphire femtosecond (fs) laser system (Spectra-Physics) was employed to excite the NTRT-PL. The excitation was achieved using laser beams with a central wavelength of 266 nm, obtained through the sum frequency of 800 nm and 400 nm fs laser beams using a beta-$BaB_2O_4$ (barium metaborate) crystal. The laser pulses had a duration of 130 fs, a repetition rate of 1 kHz, and a spot size of 1 mm. The PL emission was captured by a spectrometer (Bruker Optics 250 IS/SM) coupled with an intensified charge-coupled device (CCD) detector (IStar 740, Andor). For nanosecond time-resolved experiments, the delay time of the CCD shutter was adjusted. A laser pulse served as an external trigger signal to open the temporal gates of the intensified CCD (100 ms and 0.5 ns) through a synchronization/delay generator (SDG) and digital delay/pulse generator (DG 535). This allowed the recording of transient PL spectra at different decay times by the CCD detector. Scheme 2 illustrates the experimental setup in a schematic diagram. The time-resolved photoluminescence (TRPL) data were measured using a custom-built single photon counting system. In this system, a picosecond pulsed diode laser ($\lambda_{ex} = 375$ nm, PicoQuant, LDH-P-C-375) with a pulse full width at half maximum of less than 40 ps was utilized as the excitation source. The signals emitted were dispersed using a grating spectrometer, detected by a high-speed photomultiplier tube, and then correlated using a single photon counting card.

The performance tests related to PEC properties were conducted using a CHI660E electrochemical workstation (Chenhua, Shanghai) equipped with a standard three-electrode cell. The working electrode consisted of the prepared specimens, a platinum foil served as the counter electrode, and a saturated Ag/AgCl electrode used as the reference electrode. For the measurement of transient photocurrent density versus time curves, an aqueous solution of 0.1 M $Na_2SO_4$, saturated with $N_2$, was employed as the electrolyte. The selected sample working electrodes were illuminated from the front side under AM 1.5G chopped irradiation provided by a solar simulator (SS150A, ZOLIX) with an intensity of 100 mW/cm$^2$. The applied potential was maintained at a constant value of 0 V versus Ag/AgCl. In addition, a 0.2 M $Na_2SO_4$ solution was used as the electrolyte for acquiring electrochemical impedance spectra (EIS) plots. The EIS measurements were performed using a 300 W xenon lamp as a simulated AM 1.5G solar light source with an intensity of 100 mW/cm$^2$. Unless specifically mentioned, all potentials in this study were referenced to the normal hydrogen electrode (NHE) and were calculated based on the potentials obtained from the Ag/AgCl electrode using the equation: $E_{NHE} = E_{Ag/AgCl} + 0.1976V$. A platinum plate counter electrode was employed during these measurements.

### 2.5. Photodegradation of MO

Furthermore, the photocatalytic activities of the binary and ternary heterostructure films were investigated through the photodegradation of MO under a standard solar simulator (AM 1.5) powered by a 300 W tungsten halogen lamp, providing simulated UV-Visible light irradiation. Additionally, the photodegradation performances of all as-prepared specimens were performed using MO as the model compound under near infrared light (NIR) irradiation, which supported by a 500 W xenon lamp plus a CUT780 cut-off filter to simulate NIR (780 nm – 2500 nm). The reaction temperature of light source was controlled at 25°C with a water bath. All chemicals used were of analytical grade, and aqueous solutions were prepared using ultrapure water (Milli-Q, Millipore). A solution of MO (3 mg) was dissolved in 200 mL of deionized water, resulting in a concentration of 15 mg/L. The supernatant was then transferred to a quartz cuvette to measure its absorption spectrum. The MO solution containing the catalyst was subjected to UV-Visible and NIR irradiations for various durations at room temperature. The concentration of the MO solution was monitored every 20 minutes using a UV-Vis spectrophotometer by tracking the intensity variation of the characteristic absorption peak at 465 nm. To detect the reactive species during photocatalytic degradation, trapping experiments were conducted using a 2 mM methanol aqueous solution to capture holes ($h^+$) and a 2 mM isopropanol (IPA) solution to scavenge hydroxyl radicals (•OH). Additionally, $N_2$ bubbling was employed to inhibit the superoxide radical (•$O_2^-$). The photocatalytic conditions remained consistent with the aforementioned experiments.

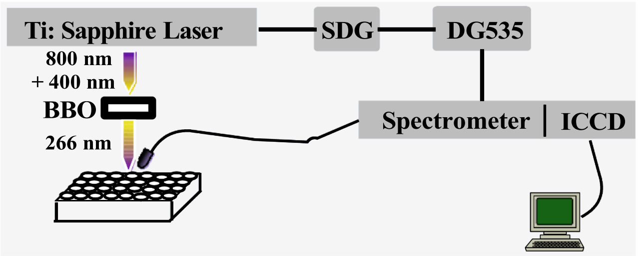

**Scheme 2.** Experiment setup of nanosecond time-resolved transient PL (NTRT-PL) measurements.

## 3. Results and discussions

The surface morphology and cross-sectional features of the synthesized specimens were characterized using SEM, as depicted in Figure 1. Figure 1(a) presented a top-view SEM image of pristine $TiO_2$ annealed at 450°C in an atmospheric environment. The image vividly demonstrates the synthesized $TiO_2$ exhibiting a nanorods shape with a diameter of approximately 20 nm and a length around of 100 nm, which is in good agreement with the SEM image of a magnified cross-section of a single $TiO_2$ nanotube. In Figure 1(b), the bare BiOI material is displayed, exhibiting a two-dimensional (2D) irregular flower-like structure composed of lamellar nanoflakes with a thickness of approximately 20 nm and a diameter of 260 nm. The 2D nanoflakes structure of BiOI is formed and calcined at 200°C under an air atmosphere, where $[Bi_2O_2]^{2+}$ slabs of BiOI are interleaved with two $I^-$ slabs. Furthermore, the surface of BiOI-NFs was decorated with Au-NPs using an ion sputtering method. The inset of Figure 1(b) shows the morphology of BiOI-NFs after the Au deposition process with a sputtering period of 30 s. Clearly, numerous Au-NPs with an average particle size of approximately 25 nm are present on the surfaces and edges of BiOI-NFs. Moving on to Figure 1(c), the microstructure of $TiO_2$-NRAs/BiOI-NFs is displayed, where strip-like BiOI structures have grown on the surfaces of $TiO_2$-NRAs, indicating the formation of hierarchical heterostructures. Upon magnification, the illustration in Figure 1(d) reveals the randomly oriented BiOI-NFs with dimensions of about 40 nm × 120 nm, exhibiting variable gaps among $TiO_2$-NRAs. This not only enhances the contact at the interface between BiOI-NFs and $TiO_2$-NRAs but also creates mesopores on the surface of the $TiO_2$-NRAs/BiOI-NFs nanocomposites. These mesopores are believed to provide more interfacial charge transfer routes and active adsorption sites during PEC measurements. Additionally, as shown in Figure 1(e), the vertical-view SEM image of the prepared $TiO_2$-NRAs/BiOI-NFs/Au-NPs structure displays hierarchically interconnected microstructures of BiOI-NFs stagger-stacked on the surface of $TiO_2$-NRAs, with numerous uniformly discrete white dots (i.e., Au-NPs) decorating the film's surface. Upon further amplification, the morphology characterization of the ternary $TiO_2$-NRAs/BiOI-NFs/Au-NPs hybrids, as depicted in Figure 1(f), clearly reveals the irregularly sized BiOI-NFs firmly attached to the $TiO_2$-NRAs, with some small Au-NPs of approximately 25 nm appearing on both the BiOI-NFs and $TiO_2$-NRAs. Notably, the Au-NPs embedded between the BiOI-NFs and $TiO_2$-NRAs act as intermediates for facilitating Z-scheme CT. Moreover, the tightly bonded

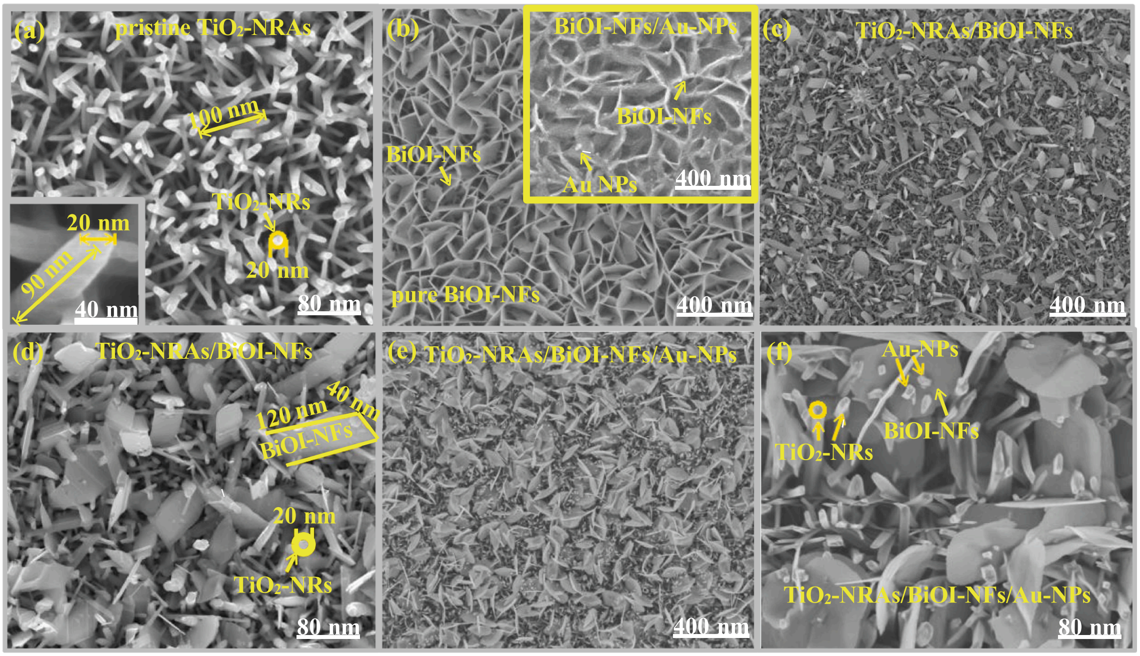

**Figure 1.** Scanning electron microscope (SEM) of (a) top-view of pristine $TiO_2$ nanorods arrays ($TiO_2$-NRAs), and the inset is cross-sectional of SEM picture for single $TiO_2$ nanorod; (b) top-view of pure BiOI nanoflakes (BiOI-NFs) films, and the inset is morphological characterization of BiOI-NFs/Au-NPs nanocomplex; (c) top-view for as-formed binary $TiO_2$-NRAs/BiOI-NFs nanocomposites; (d) high-resolution SEM picture of $TiO_2$-NRAs/BiOI-NFs binary nanocomposites; (e) vertical-view SEM picture of as-fabricated ternary $TiO_2$-NRAs/BiOI-NFs/Au-NPs nanohybrids; (f) high-resolution SEM picture of $TiO_2$-NRAs/BiOI-NFs/Au-NPs ternary nanohybrids

hierarchical ternary heterogeneous structure of $TiO_2$-NRAs/BiOI-NFs/Au-NPs promotes more efficient separation of photoinduced carriers and provides a greater number of active sites for reacting with target molecules.

The XRD patterns of the five prepared samples, namely pristine $TiO_2$-NRAs, pure BiOI-NFs, BiOI-NFs decorated with Au-NPs, $TiO_2$-NRAs/BiOI-NFs binary nanocomposites, and ternary $TiO_2$-NRAs/BiOI-NFs/Au-NPs nanohybrids, were recorded to confirm their structure, composition, and crystallinity, as shown in Figure 2(a)-(e) respectively. All XRD plots exhibit narrow and sharp diffraction peaks without any additional peaks, indicating the excellent crystalline nature of the synthesized samples. Figure 2(a) displays the XRD pattern of pristine

$TiO_2$-NRAs, where six diffraction peaks labeled with '●' correspond to (101), (004), (200), (105), (211), and (204) planes of anatase $TiO_2$ phase (JCPDS Card No. 21-1272) at $2\theta = 25.3^o$, $37.8^o$, $48.2^o$, $53.9^o$, $55.1^o$, and $62.7^o$, respectively. In Figure 2(b), the XRD pattern of pure BiOI-NFs (labeled with '▾') reveals characteristic peaks of tetragonal BiOI phase (JCPDS Card 10-0445) at $2\theta = 29.6^o$, $31.7^o$, $45.5^o$, $51.4^o$, $55.3^o$, and $66.1^o$, corresponding to (102), (110), (020), (114), (212), and (220) lattice planes, respectively. Figure 2(c) shows the XRD spectra of BiOI-NFs/Au-NPs binary nanocomplex. It displays all the diffraction peaks of tetragonal BiOI phase, along with an additional peak marked with '◆' at $44.5^o$, which matches the expected position of the deposited noble metal. This peak can be attributed to the (200) cubic phase of Au-NPs (JCPDS Card 04-0784), confirming the successful synthesis of the binary BiOI-NFs/Au-NPs metal-semiconductor (M-S) nanoheterojunctions. The stronger intensity of the diffraction peak at $31.7^o$ in the BiOI-NFs/Au-NPs sample compared to bare BiOI-NFs indicates the beneficial effect of Au-NPs decoration in promoting the generation of $V_o$ defects in BiOI. (Qu et al., 2022) The XRD patterns of $TiO_2$-NRAs/BiOI-NFs and $TiO_2$-NRAs/BiOI-NFs/Au-NPs are depicted in Figure 2(d)-(e). Apart from the diffraction peak at $55.1^o$ corresponding to (211) plane of $TiO_2$, most of the diffraction peaks for anatase $TiO_2$-NRAs and tetragonal BiOI-NFs are present without any impurity peaks. The XRD pattern of $TiO_2$-NRAs/BiOI-NFs/Au-NPs also shows the Au diffraction peak at $44.5^o$. These results indicate the sequential deposition of tetragonal BiOI-NFs and Au-NPs onto the surface of $TiO_2$-NRAs, confirming the successful construction of binary $TiO_2$-NRAs/BiOI-NFs and ternary $TiO_2$-NRAs/BiOI-NFs/Au-NPs nanoheterostructures with high purity.

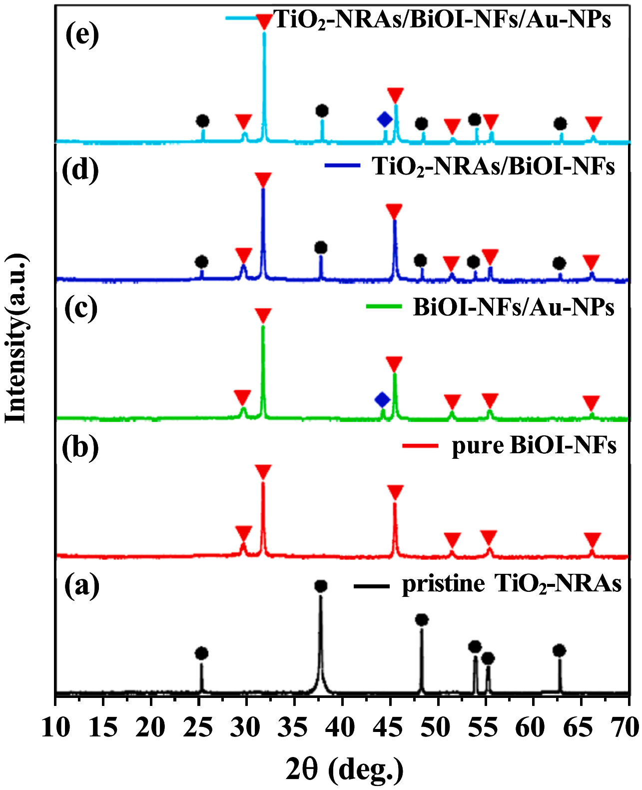

**Figure 2.** X-ray diffraction (XRD) patterns for pristine $TiO_2$-NRAs (a), (b) pure BiOI-NFs, (c)-(d) severally BiOI-NFs/Au-NPs, and $TiO_2$-NRAs/ BiOI-NFs binary nanocomposites; (e) ternary $TiO_2$-NRAs/ BiOI-NFs/Au-NPs nanohybrids.

Furthermore, it is noteworthy that the diffraction peak intensity of $TiO_2$ in the spectra of binary and ternary nanohybrids is reduced compared to pure $TiO_2$-NRAs. This can be attributed to the presence of the deposited BiOI-NFs layer, which weakens the intensity of the $TiO_2$ diffraction signal from the substrate. (Shao et al., 2021)

The Raman spectra, obtained by exciting the samples with a 532-nm laser and covering a wave number range from 60 $cm^{-1}$ to 220 $cm^{-1}$, provide valuable insights into the composition, crystalline quality, and formation of $V_o$ defects in the prepared binary and ternary nanohybrids, as showcased in Figure 3. Each Raman peak corresponds to specific molecular vibrations and helps identify the characteristics of the synthesized nanohybrids. Figure 3(a) exhibits the Raman spectrum of pristine $TiO_2$-NRAs. The stronger and weaker peaks observed at 144.5 $cm^{-1}$ and 199.6 $cm^{-1}$, respectively, correspond to the Raman active $E_g$ mode of anatase $TiO_2$. (Mohamed et al., 2021) In Figure 3(b), the Raman spectrum of pure BiOI-NFs obtained through solid-state synthesis displays two prominent peaks located at 85.3 $cm^{-1}$ and 150.1 $cm^{-1}$. These peaks correspond to the stretching

vibrations of the internal Bi-I bond in BiOI, specifically the $E_g$ and $A_{1g}$ modes, respectively. (Qu et al., 2022) This confirms the successful formation of BiOI. Comparing it with the spectrum of pure BiOI-NFs, the vibrational bands in BiOI-NFs/Au-NPs (Figure 3(c)) have experienced red shifts to 89.7 $cm^{-1}$ and 150.3 $cm^{-1}$, respectively, indicating the interaction and bonding between BiOI and Au. Additionally, the intensities of both Raman peaks in BiOI-NFs/Au-NPs noticeably decrease and broaden, suggesting the presence of a higher concentration of $V_o$ defects in BiOI and a decrease in crystallinity. (Kumara et al., 2022) After the formation of nanoheterostructures, the Raman spectra of $TiO_2$-NRAs/BiOI-NFs and $TiO_2$-NRAs/BiOI-NFs/Au-NPs (Figure 3(d) and (e)) show the characteristic bands of both BiOI and $TiO_2$, confirming the successful synthesis of the binary and ternary nanoheterojunctions, which aligns with the SEM results. No additional peaks are observed, indicating the absence of impurities. However, the Raman vibrational bands at 86.7 $cm^{-1}$ and 150.5 $cm^{-1}$ in $TiO_2$-NRAs/BiOI-NFs have red-shifted to 86.9 $cm^{-1}$ and 150.7 $cm^{-1}$, respectively, in $TiO_2$-NRAs/BiOI-NFs/Au-NPs. These shifts correspond to the stretching vibration modes of $E_g$ and $A_{1g}$, suggesting a weaker bond strength in the nano-heterojunctions of $TiO_2$-NRAs/BiOI-NFs/Au-NPs compared to $TiO_2$-NRAs/BiOI-NFs. (Yamamura et al., 2022) Moreover, the Raman peak intensities are lower for $TiO_2$-NRAs/BiOI-NFs compared to pure BiOI-NFs, and the two main peaks at 86.7 $cm^{-1}$ and 150.5 $cm^{-1}$ are noticeably broadened, indicating a deterioration in crystallization quality. This deterioration can be attributed to the presence of $V_o$ defects in the binary nanoheterojunctions. This effect is even more pronounced in the $TiO_2$-NRAs/BiOI-NFs/Au-NPs nanohybrids, confirming the formation of a higher concentration of $V_o$ defects compared to the binary nanocomplex, which leads to a decrease in crystallinity. (Kaur et al., 2021)

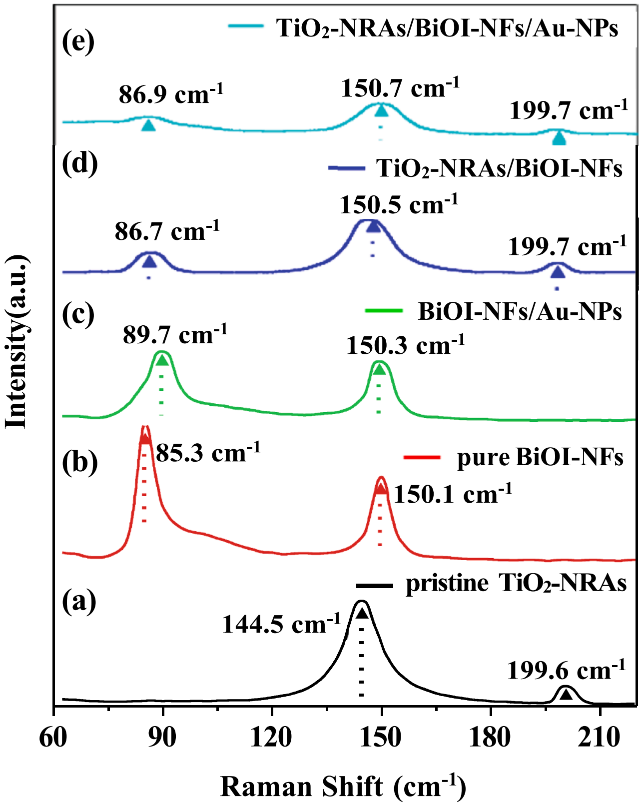

**Figure 3.** Raman spectra of (a) pristine $TiO_2$-NRAs, (b) pure BiOI-NFs films, (c)-(d) respective BiOI-NFs/Au-NPs, and $TiO_2$-NRAs/BiOI-NFs dual nanocomplex; (e) ternary $TiO_2$-NRAs/BiOI-NFs/Au-NPs nanohybrids.

UV-vis DRS measurements were employed as a valuable complementary technique to XRD and Raman to assess the optical absorption properties and band-gap energies ($E_g$) of the single, binary, and ternary specimens, which play a crucial role in determining the PEC performance. Figure 4(a) illustrates the distinct spectra obtained for pristine $TiO_2$-NRAs (black line), revealing a characteristic absorption edge below 400 nm and an inadequate response to visible light. Conversely, the separated BiOI-NFs specimen (red line) exhibited a strong response to visible light, with an absorption edge around 670 nm. Both absorption edges arise from electronic transitions within the intrinsic band gap. Furthermore, the binary BiOI-NFs/Au-NPs (green line) and $TiO_2$-NRAs/BiOI-NFs (blue line) nanocomposites displayed enhanced absorption intensity in the visible light range. This enhanced absorption is beneficial for generating more $e^-$ - $h^+$ pairs and thereby improving the PEC performance, confirming the successful synthesis of the

nano-heterostructures as intended. Importantly, with the incorporation of Au-NPs on $TiO_2$-NRAs/BiOI-NFs, the absorption edge of the $TiO_2$-NRAs/BiOI-NFs/Au-NPs sample (cyan line) significantly extended into a longer wavelength region (approximately 760 nm) compared to $TiO_2$-NRAs/BiOI-NFs. This extension can be attributed to the synergistic effect of the heterostructure formed by abundant $V_o$ defects and Au-NPs embedded in $TiO_2$-NRAs/BiOI-NFs. Notably, the absorption curve of $TiO_2$-NRAs/BiOI-NFs/Au-NPs exhibited a distinct bulge near 565 nm, analogous to the LSPR absorption peak of Au-NPs. (Güntner and Schenk, 2023) The $E_g$ values of the prepared specimens can be estimated using the equation: $\alpha h\nu = A(h\nu - E_g)^{n/2}$, where A is a proportionality constant, $\alpha$ is the absorption coefficient, $h\nu$ is the incident photon energy, and $E_g$ is the band-gap energy of the material. The value of n determines the transition type of the semiconductor, with n= 1 indicating a direct semiconductor and n = 4 indicating an indirect semiconductor. Both $TiO_2$ and BiOI are direct semiconductors, so the value of n is 1. (Liao et al., 2022) Therefore, the $E_g$ values of the prepared specimens can be estimated from the tangent intercept of the $(\alpha h\nu)^{1/2}$ and ($h\nu$) curves. As shown in Figure 4(b), the $E_g$ values for pristine $TiO_2$-NRAs, pure BiOI-NFs, BiOI-NFs/Au-NPs, $TiO_2$-NRAs/BiOI-NFs, and $TiO_2$-NRAs/BiOI-NFs/Au-NPs are determined to be 3.11 eV, 1.85 eV, 1.76 eV, 1.72 eV, and 1.63 eV, respectively. It is evident that the $E_g$ values of the binary and ternary nano-composites are smaller than those of the individual semiconductors due to the formation of nano-heterostructures. This phenomenon promotes the generation of more photogenerated carriers and improves the utilization of light.

To investigate the chemical bonding states and surface defect states, XPS survey spectra were conducted on the prepared specimens. The full range survey XPS spectra (0 eV - 1100 eV) were analyzed to determine the dominant elements in the $TiO_2$-NRAs/BiOI-NFs/Au-NPs nanoheterojunctions, with pristine $TiO_2$-NRAs serving as a reference. The results, shown in Figure S1(a) (Supporting Information, SI), clearly indicate the presence of Ti, O, and C peaks in the XPS survey scan of $TiO_2$-NRAs, which are typical elements of $TiO_2$, except for the $C_{1s}$ peak originating from carbon impurities. In addition to Ti, O, and C peaks, the XPS survey scan of $TiO_2$-NRAs/BiOI-NFs/Au-NPs prominently reveals

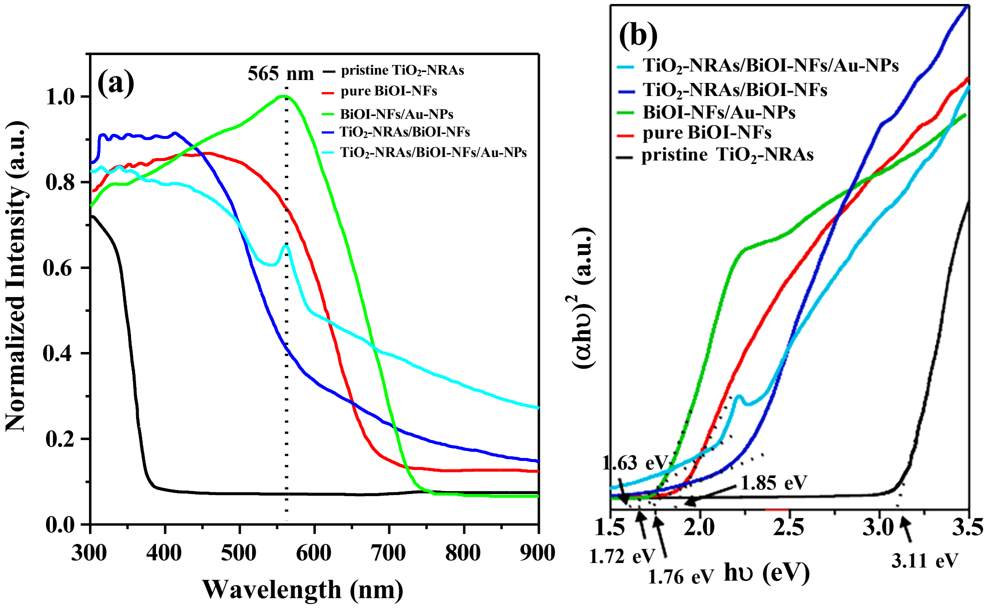

**Figure 4.** UV-visible diffuse reflectance spectra for as-prepared specimens (a) and (b) derived Tauc plots for optical band-gap of pristine $TiO_2$-NRAs, pure BiOI-NFs, binary BiOI-NFs/Au-NPs nanocomposites, $TiO_2$-NRAs/BiOI-NFs dual nanocomplex, and $TiO_2$-NRAs/BiOI-NFs/Au-NPs ternary nanohybrids, respectively.

the dominant elements Bi, I, and Au, confirming the formation of the ternary $TiO_2$-NRAs/BiOI-NFs/Au-NPs hetero-nanostructures. This finding is consistent with the experimental results obtained from SEM, XRD, and UV-vis DRS tests. Notably, the XPS signal intensity of Ti in the $TiO_2$-NRAs/BiOI-NFs/Au-NPs sample is weaker compared to that in pristine $TiO_2$-NRAs. This can be attributed to the obstruction of the $TiO_2$-NRAs substrate by the top BiOI-NFs narrow bandgap semiconductor layer. (Shao et al., 2021) To further investigate the evidence of surface defects related to $V_o$ in pristine and decorated $TiO_2$-NRAs, which significantly influence the CT process and the PEC performance, we analyzed the chemical components and bonding configurations using high-resolution XPS measurements (HR-XPS). Specifically, Figure S1(b) (SI) presents the HR-XPS of the Ti 2p core level for pristine $TiO_2$-NRAs, binary $TiO_2$-NRAs/BiOI-NFs, and ternary $TiO_2$-NRAs/BiOI-NFs/Au-NPs nanohybrids. The experimental data (black, blue, and cyan lines, respectively) were fitted with different curves (black and red solid lines) using a mixed Gaussian-Lorentzian function, which provided optimized fitting results. The fitted curves included $Ti^{3+}2p_{3/2}$, $Ti^{4+}2p_{3/2}$, $Ti^{3+}2p_{1/2}$, and $Ti^{4+}2p_{1/2}$, corresponding to the core levels of $Ti^{3+}$ and $Ti^{4+}$. In the pure $TiO_2$-NRAs sample, two Ti 2p XPS peaks were observed at BE of 459.0 eV and 464.7 eV, which can be attributed to Ti $2p_{3/2}$ and Ti $2p_{1/2}$ from the Ti-O bond, respectively, (Huang et al., 2023) indicating the presence of $Ti^{4+}$. Similarly, the $TiO_2$-NRAs/BiOI-NFs sample exhibited two peaks at 458.4 eV and 464.2 eV, corresponding to Ti $2p_{3/2}$ and Ti $2p_{1/2}$ due to spin orbit-splitting. (Liu et al., 2022) The Ti 2p core level spectrum of the $TiO_2$-NRAs/BiOI-NFs/Au-NPs sample centered at 458.7 eV and 464.4 eV was assigned to Ti $2p_{3/2}$ and Ti $2p_{1/2}$, respectively, (Yang et al., 2023) consistent with $Ti^{4+}$ in the $TiO_2$ lattice. Moreover, the Ti 2p core level peaks of $TiO_2$-NRAs/BiOI-NFs and $TiO_2$-NRAs/BiOI-NFs/Au-NPs shifted to lower energy states compared to pristine $TiO_2$-NRAs, indicating an enhanced electron screening effect resulting from increased electron density in $TiO_2$. (Krishna and Philip, 2022) This shift can be attributed to the different energy positions of the $E_F$ among $TiO_2$; BiOI, and Au, which are -4.7 eV (vs. vacuum level, $E_{vac}$), -4.4 eV (vs. $E_{vac}$), and -5.1 eV (vs. $E_{vac}$), respectively. (Mao et al., 2023; Wang et al., 2022; Wang et al., 2023) This causes electron transfer from BiOI to $TiO_2$ and subsequent implantation into Au-NPs. Furthermore, through mixed function fitting, it is evident that the BE values corresponding to various oxidation states of Ti atoms can be distinguished. Peaks located at 458.8 eV, 458.9 eV, 459.1 eV, 464.4 eV, 464.5 eV, and 465.0 eV are attributed to the $Ti^{4+}$ valence state, (Shao et al., 2014) while peaks at 458.3eV and 458.5 eV can be assigned to the $Ti^{3+}$ valence state. (Shao et al., 2014; Zhao et al., 2021) The presence of $Ti^{3+}$ in the $TiO_2$-NRAs/BiOI-NFs/Au-NPs nanoheterojunctions suggests the formation of $V_o$ defects in the $TiO_2$-NRAs lattice. (Wang et al., 2022) We presented the surface atomic $Ti^{3+}/Ti^{4+}$ ratios of the pristine $TiO_2$-NRAs, binary $TiO_2$-NRAs/BiOI-NFs, and ternary $TiO_2$-NRAs/BiOI-NFs/Au-NPs nano-heterojunctions by calculating the integral fitting of the peak areas in Table S1 (SI), which directly correspond to the concentrations of $V_o$ defects and stoichiometric $TiO_2$. We can explicitly observed that the surface atomic ratios $Ti^{3+}/Ti^{4+}$ are 0.906, 1.04, and 1.19 for the specimens of pristine $TiO_2$-NRAs, $TiO_2$-NRAs/BiOI-NFs, and $TiO_2$-NRAs/BiOI-NFs/Au-NPs, respectively. The experimental results further confirmed that the nano-heterostructures constructed by depositing BiOI-NFs and Au-NPs on $TiO_2$-NRAs are more conducive to the generation of $V_o$ defects, which could provided a greater number of energetic electrons and promoted the electrical conductivity and electron mobility of nano-system. (Shao et al., 2022) As depicted in Figure S1(c) (SI), we present the HR-XPS of the Bi 4f core level for the pristine BiOI-NFs, $TiO_2$-NRAs/BiOI-NFs, and $TiO_2$-NRAs/BiOI-NFs/Au-NPs samples. The HR-XPS analysis of the Bi 4f core level in the pure BiOI-NFs films reveals two distinct peaks at 159.0 eV and 164.3 eV, corresponding to the Bi $4f_{7/2}$ and Bi $4f_{5/2}$ orbitals, respectively (Yin et al., 2023). Similarly, the Bi 4f peaks for $TiO_2$-NRAs/BiOI-NFs appear at 159.4 eV and 164.7 eV, which are consistent with the Bi $4f_{7/2}$ and Bi $4f_{5/2}$ components of BiOI. (Li et al., 2022) Furthermore, the high-resolution Bi 4f spectra of $TiO_2$-NRAs/BiOI-NFs/Au-NPs nanoheterojunctions exhibit peaks located at 158.7 eV and 164.0 eV for Bi $4f_{7/2}$ and Bi $4f_{5/2}$, respectively. (Zhang et al., 2021) It is noteworthy that the separation between the Bi 4f spin orbits remains constant at 5.3 eV across all the BiOI-related nano-systems, indicating the trivalent oxidation state of the Bi element. Comparing the pristine BiOI-NFs sample, the Bi $4f_{7/2}$ and Bi $4f_{5/2}$ signals for $TiO_2$-NRAs/BiOI-NFs and $TiO_2$-NRAs/BiOI-NFs/Au-NPs show slight shifts towards higher and lower BE values, respectively, providing evidence of interfacial interaction in the nano-heterostructures. Moving on to Figure S1(d) (SI), the I 3d peaks for pure BiOI-NFs are observed at 618.8 eV and 630.3 eV, corresponding to I $3d_{5/2}$ and I $3d_{3/2}$ core levels, respectively. (Prusty et al., 2022) Similarly, the $TiO_2$-NRAs/BiOI-NFs sample displays an intense doublet at 619.2 eV and 630.7 eV, indexing the photoelectron emission from the I $3d_{5/2}$ and I $3d_{3/2}$ core levels, with no XPS peak indicating iodine vacancies. (Wang et al., 2022) In contrast, the XPS spectrum of I element in $TiO_2$-NRAs/BiOI-NFs/Au-NPs exhibits peaks at BE values of 618.6 eV and 630.1 eV, corresponding to I $3d_{5/2}$ and I $3d_{3/2}$ electron orbitals in BiOI. (Xu et al., 2022) Notably, the BE values of Bi 4f and I 3d core levels for $TiO_2$-NRAs/BiOI-NFs are shifted to higher values compared to pure

BiOI-NFs, suggesting electron migration from BiOI-NFs to $TiO_2$-NRs due to the different $E_F$ values between BiOI and $TiO_2$. Conversely, the BE values of Bi 4f and I 3d spin-orbit interactions for $TiO_2$-NRAs/BiOI-NFs/Au-NPs are shifted to lower BE values relative to pure BiOI-NFs films, indicating electron transfer to the BiOI component, possibly originating from the injection of “hot electrons” from adjacent Au-NPs induced by the LSPR effect. (Yu et al., 2021) To confirm the electron transfer behavior among the various components in the nano-heterostructures, we performed deconvolution of the Au 4f envelope in the Au-NPs-containing coatings. As shown in Figure S1(e) (SI), pristine BiOI-NFs with deposited Au-NPs exhibit two intensity peaks at 87.4 eV and 83.7 eV, assigned to the Au $4f_{5/2}$ and Au $4f_{7/2}$ spin-orbit coupling of Au, respectively. (Wu et al., 2023) In the case of $TiO_2$-NRAs/BiOI-NFs/Au-NPs, the Au 4f core level shows two characteristic peaks at 84.0 eV and 87.7 eV for Au $4f_{7/2}$ and Au $4f_{5/2}$, respectively. (Wu et al., 2023) Comparing these values with the characteristic peaks of $Au^0$ at 83.6 eV (Au $4f_{7/2}$) and 87.2 eV (Au $4f_{5/2}$), (Silva et al., 2019) we observe a clear shift of 0.1 eV - 0.5 eV towards higher BE values for the Au 4f of Au-NPs in theBiOI-NFs/Au-NPs and $TiO_2$-NRAs/BiOI-NFs/Au-NPs samples. This shift indicates that after combination, the Au-NPs are more likely to transfer hot electrons to neighboring semiconductors, primarily due to the LSPR effect facilitated by the close connection between the Au-NPs and $TiO_2$-NRAs/BiOI-NFs. This electron transfer is beneficial for the efficient transfer of electrons and plays a crucial role in the PEC reaction.

To further confirm the presence of $V_o$ defects in the surface region of the prepared binary and ternary nano-heterostructures, we conducted an analysis of the HR-XPS spectra of the O 1s core-level signals. Figure 5(a) represents the XPS spectrum of the O1s peak for the tested samples before curve fitting. Figure 5(b) shows the XPS spectrum of the O1s peak for the as-prepared specimens after curve fitting, along with a comprehensive explanation of the differences and effectiveness between the spectra before and after O1s curve fitting. By employing Gaussian function fitting, we deconvoluted the spectra into three components corresponding to different oxygen species: lattice oxygen ($L_o$), $V_o$, and adsorbed oxygen ($A_o$). The characteristic peaks for these species were observed at 529.7 eV - 530.3 eV, (Ji et al., 2023) 530.9 eV -531.6 eV, (Liu et al., 2015; Li et al., 2022) and 532.1 eV - 532.4 eV, (Lu et al., 2023; An et al., 2022) respectively. To provide a clear understanding of the influence of heterojunction construction and Au-NPs deposition on the formation of $V_o$ defects, we summarized the estimated $V_o/(L_o + A_o)$ molar ratios of the O 1s XPS spectra for the pristine, binary, and ternary nano-heterostructures in Table S2 (SI). The molar ratios were determined by analyzing the peak areas of the three components: $L_o$, $V_o$, and $A_o$. Among the samples, the $TiO_2$-NRAs/BiOI-NFs/Au-NPs nano-heterostructure exhibited the highest $V_o/(L_o + A_o)$ molar ratio of 0.367, followed by $TiO_2$-NRAs/BiOI-NFs with a ratio of 0.313. The BiOI-NFs/Au-NPs sample displayed a molar ratio of 0.186, while pristine $TiO_2$-NFs and separated BiOI-NFs exhibited lower values of 0.109 and 0.087, respectively. By synthesizing and comparing the above results, we observed that the concentration of $V_o$ defects in the ternary $TiO_2$-NRAs/BiOI-NFs/Au-NPs nano-heterostructures was higher than that in $TiO_2$-NRAs/BiOI-NFs. This trend is similar to the variation observed in the surface atomic ratios of $Ti^{3+}/Ti^{4+}$, which can be attributed to the synergistic effect between nanoheterostructures construction and the presence of Au-NPs, as anticipated.

Steady-state PL spectroscopy is widely recognized as an effective method for gaining further understanding of the electronic structure and characteristics of active sites located on the surfaces or interfaces of binary and ternary nano-heterojunctions. This non-destructive technique can offer valuable information regarding the presence of surface $V_o$ defects, as well as the efficiency of processes such as charge carriers trapping, migration, and recombination. In comparison to the variation in absolute intensity of PL, we place more emphasis on the variations in the steady-state PL spectral weight and features. Figure 6(a-e) shows the steady-state PL of various samples, including pristine $TiO_2$-NTAs, pure BiOI-NFs films, BiOI-NFs/Au-NPs, $TiO_2$-NRs/BiOI-NFs, and $TiO_2$-NRs/

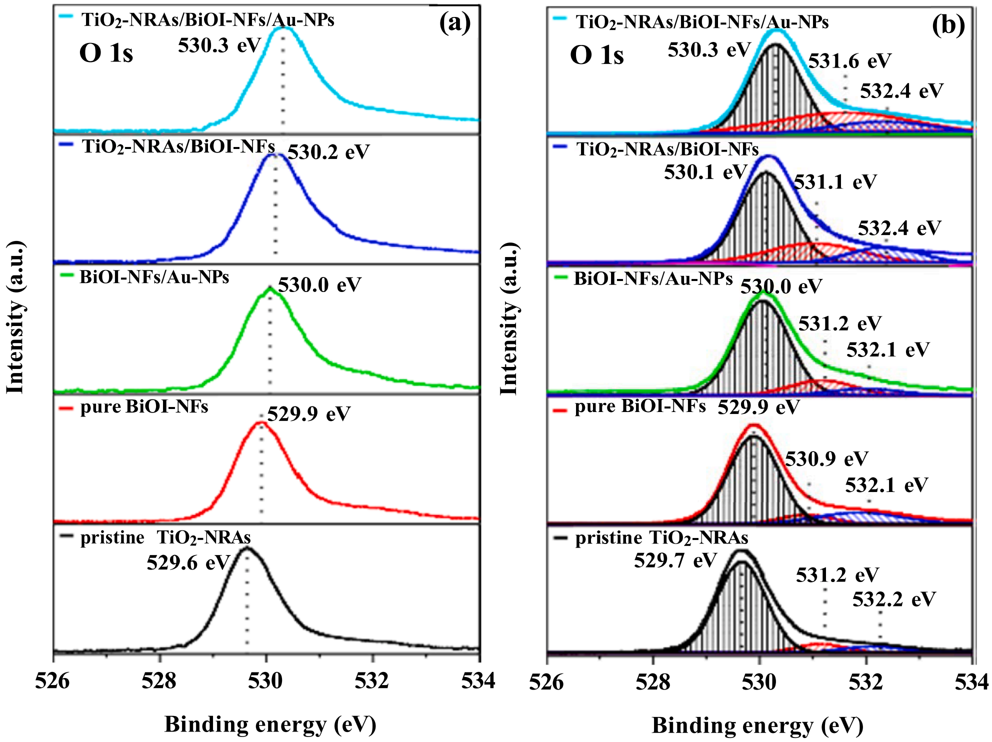

**Figure 5.** The high-resolution XPS spectra of O 1s before (a) and after (b) element fitting for the thus-obtained specimens, respectively.

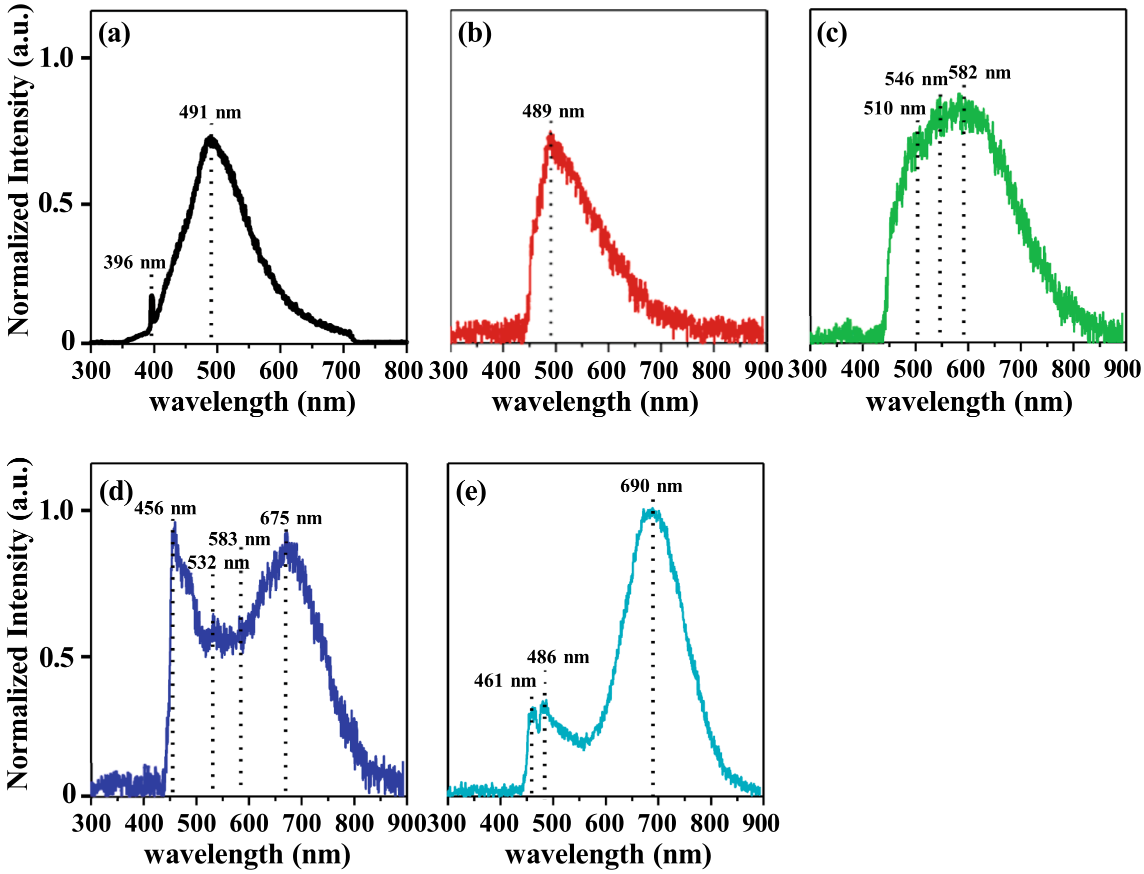

**Figure 6.** (a-e) Steady-state PL spectra of pristine $TiO_2$-NRAs, pure BiOI-NFs, BiOI-NFs/Au-NPs, $TiO_2$-NRs/BiOI-NFs, and $TiO_2$-NRs/BiOI-NFs/Au-NPs nano-heterostructures excited by 266 nm femtosecond pulse, respectively.

BiOI-NFs/Au-NPs nano-heterojunctions, when excited by a 266 nm fs pulse at ambient temperature. As illustrated in Figure 6(a), the steady-PL spectrum of pristine $TiO_2$-NRAs exhibited weak emission strength at 396 nm and conspicuous emission intensity at 491 nm, which correspond to the band-to-band emission and the indirect radiative transition of self-trapped electrons from $V_o$ defects to holes in the $TiO_2$-NRAs, respectively. (Zhang et al., 2023; Bopape et al., 2023)

Simultaneously, the steady-PL spectra of pure BiOI-NFs and BiOI-NFs/Au-NPs (in Figure 6(b-c)) displayed intense asymmetric wave-band emission profiles located at 489 nm, 510 nm, 546 nm, and 582 nm, which can be ascribed to the indirect radiative transition of self-trapped electrons associated with $V_o$ in BiOI-NFs. (Chen et al., 2021) Besides, the steady-state PL emission profile of the $TiO_2$-NRAs/BiOI-NFs binary nanoheterojunctions illustrated four emitted contributions sited at 456 nm, 532 nm, 583 nm, and 675 nm, spanning a range from 300 nm to 900 nm. Various researchers have validated 456 nm and 675 nm double emission peaks originated from the shallow-level and deep-level emissions caused by shallow and deep energy traps induced by surface $V_o$ defects in BiOI-NFs, respectively. (Chen et al., 2021; Sun et al., 2021) Synchronously, We inclined to believe that the other two emission peaks, located at 532 nm and 583 nm, respectively, can be attributed to the radiative transition of trapped exciton related with $V_o$ defects in $TiO_2$-NRAs. (Chen et al., 2022) Additionally, it can be distinctly observed that the steady-PL of $TiO_2$-NRs/BiOI-NFs/Au-NPs ternary nano-heterostructures presented a dramatic emission peak centered at 690 nm, resulting from the radiative transition from the CB of $TiO_2$ to the VB of BiOI; (Zhang et al., 2022) and more lower PL profiles can be seen sited at 461 nm and 486 nm, attributing to the fact that radiative transition between Au-NPs and $V_o$ defects in BiOI. (Chen et al., 2021)

Understanding the generation, transportation, trapping, and recombination processes of free carriers in semiconductor nanostructures is crucial for achieving high conversion efficiency in PEC applications. To gain insights into the CT dynamics and the fate of charge carriers at the interface, we employed NTRT-PL spectrum analysis as a real-time analytical platform. This technique provides critical information about the role of nanoheterostructures in enhancing photoconversion performance. Figure 7(a-e) illustrates the NTRT-PL spectra of the prepared binary and ternary nano-heterostructures involving BiOI-NFs, Au-NPs, and $TiO_2$-NRAs. These samples were irradiated with a monochromatic fs laser at a wavelength of 266 nm and at room temperature, with a time resolution of 1.5 ns intervals. Figure 7(a) demonstrates that the pristine $TiO_2$-NRAs sample exhibits a transient peak of PL around 3.13 eV (396 nm), which corresponds to the electronic direct transition between the VB and the CB. Additionally, the transient PL emission peaks of pure $TiO_2$-NRAs display a blue-shift phenomenon at approximately 2.49 eV (497 nm), 2.52 eV (491 nm), 2.54 eV (487 nm), 2.57 eV (482 nm), and 2.62 eV (473 nm), with decreasing intensities over time. These peaks originate from defect energy states caused by indirect radiative emissions from $V_o$ defects within the forbidden region of $TiO_2$, which is consistent with the steady-state PL spectroscopy presented in Figure 6(a). (Shao et al., 2022; Shao et al., 2021) Furthermore, Figure 7(b) showcases the NTRT-PL patterns of the pure BiOI-NFs sample, revealing five transient PL radiative peaks centered at 425 nm, 436 nm, 485 nm, 502 nm, and 519 nm, with decreasing intensities over a time evolution of 0 ns - 6 ns. These transient PL peaks are attributed to the indirect radiative recombination between the electrons in the CB and the $V_o$ defects in BiOI. The $V_o$ defects can act as trapping centers for photoexcited $h^+$, thereby facilitating charge separation and transmission. (Wang et al., 2023) Subsequently, we present the NTRT-PL spectra of the binary and ternary nanoheterostructures in Figure 7(c-e), including BiOI-NFs/Au-NPs, $TiO_2$-NRAs/BiOI-NFs, and $TiO_2$-NRAs/BiOI-NFs/Au-NPs. Figure 7(c) reveals the NTRT-PL spectra of the BiOI-

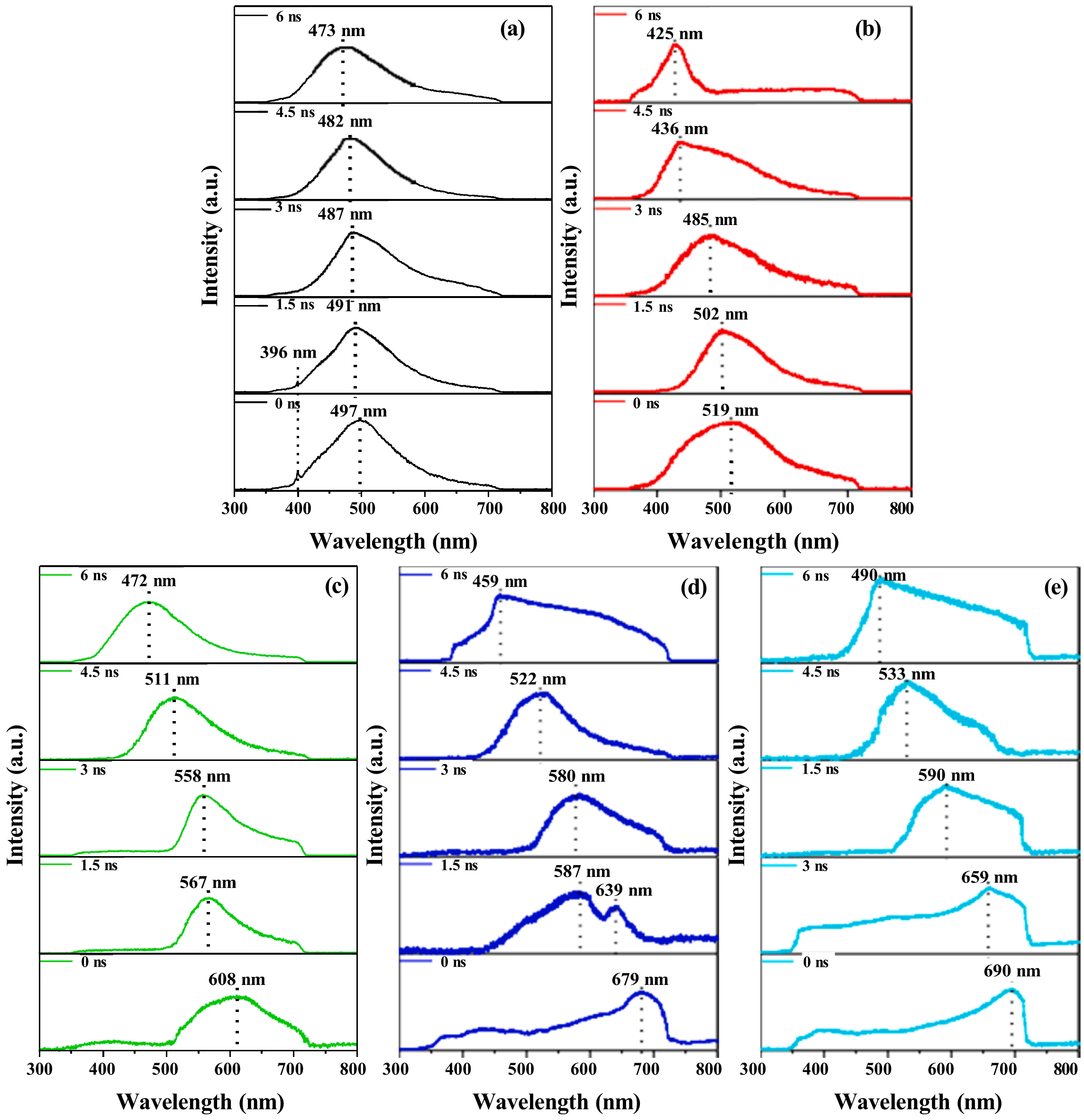

**Figure 7.** (a-e) NTRT-PL spectra of pristine $TiO_2$-NRAs, pure BiOI-NFs, BiOI-NFs/Au-NPs, $TiO_2$-NRAs/BiOI-NFs, and $TiO_2$-NRAs/BiOI-NFs/Au-NPs nano-heterojunctions irradiated by 266 nm femtosecond pulse, respectively.

NFs/Au-NPs nanocomposites, displaying transient PL profiles centered at 472 nm, 511 nm, 558 nm, 567 nm, and 608 nm. Previous research has shown that these transient PL peaks arise from radiative recombination between the hot electrons induced by the presence of Au-NPs and the $V_o$ defects in BiOI-NFs. (Fu et al., 2021) Moreover, Figure 7(d) presents the NTRT-PL spectra of the $TiO_2$-NRAs/BiOI-NFs sample, exhibiting transient PL peaks located at 459 nm, 522 nm, 580 nm, 587 nm, 639 nm, and 679 nm. Specifically, the PL emission peaks at 459 nm, 522 nm, and 639 nm can be attributed to the radiative transition between $e^-$ and V defects in BiOI, while the PL patterns centered at 580 nm and 587 nm are ascribed to the radiative relaxation from $V_o$ defects to the $h^+$ in the VB ($h^+_{VB}$) in $TiO_2$. (Chen et al., 2022) The remaining emitted peak at 679 nm (approximately 1.83 eV) mainly originates from direct radiative recombination of photogenerated $e^-$ - $h^+$ pairs in BiOI, which is in good agreement with the E value of BiOI-NFs. In Figure 7(e), the NTRT-PL spectra of the $TiO_2$-NRAs/BiOI-NFs/Au-NPs sample exhibit transient peaks at 490 nm, 533 nm, 590 nm, 659 nm, and 696 nm. We believe that the radiative recombination peaks observed at 490 nm, 533 nm, and 659 nm result from the transition between $e^-$ and V defects in BiOI-NFs. The other transient PL radiative peaks centered at 590 nm and 690 nm can be attributed to indirect transitions related to $V_o$ defects in $TiO_2$ and direct "Z-scheme" recombination between $e^-$ in TiO and $h^+$ in BiOI, which necessitates the presence of Au-NPs. The stronger PL intensities caused by defects trapping $e^-$indicate a higher concentration of surface defects. Notably, the transient PL intensities of the pure BiOI-NFs, BiOI-NFs/Au-NPs, $TiO_2$-NRAs/BiOI-NFs, and $TiO_2$-NRAs/BiOI-NFs/Au-NPs samples gradually increased at the final spectral recording time (6 ns).

Ultrafast time-resolved PL spectroscopy is an authoritative indicator tool to track the CT dynamics. On the basis of the above obtained experimental results of the NTRT-PL spectra, we presented the plausible mechanisms proposed to interpret the transient CT processes for binary and ternary nanoheterostructures under fs laser irradiation at a wavelength of 266 nm at room temperature in Figures 8 and 9. According to the aforementioned statement, the $E_g$ values of $TiO_2$-NRAs and BiOI-NFs were calculated to be 3.11 eV and 1.85 eV determined by Tauc plot (Figure 4(b)), respectively. The CB and VB potential positions of $TiO_2$-NRAs and BiOI-NFs can be calculated by the following equations: $E_{VB} = \chi - E_e + 0.5 \times E_g$, and $E_{CB} = E_{VB} - E_g$; where $E_{VB}$ represents the VB edge potential, $E_{CB}$ means the CB edge potential; $\chi$ is the electronegativity of the semiconductor, and the values of $\chi$ for $TiO_2$ and BiOI are 5.80 eV and

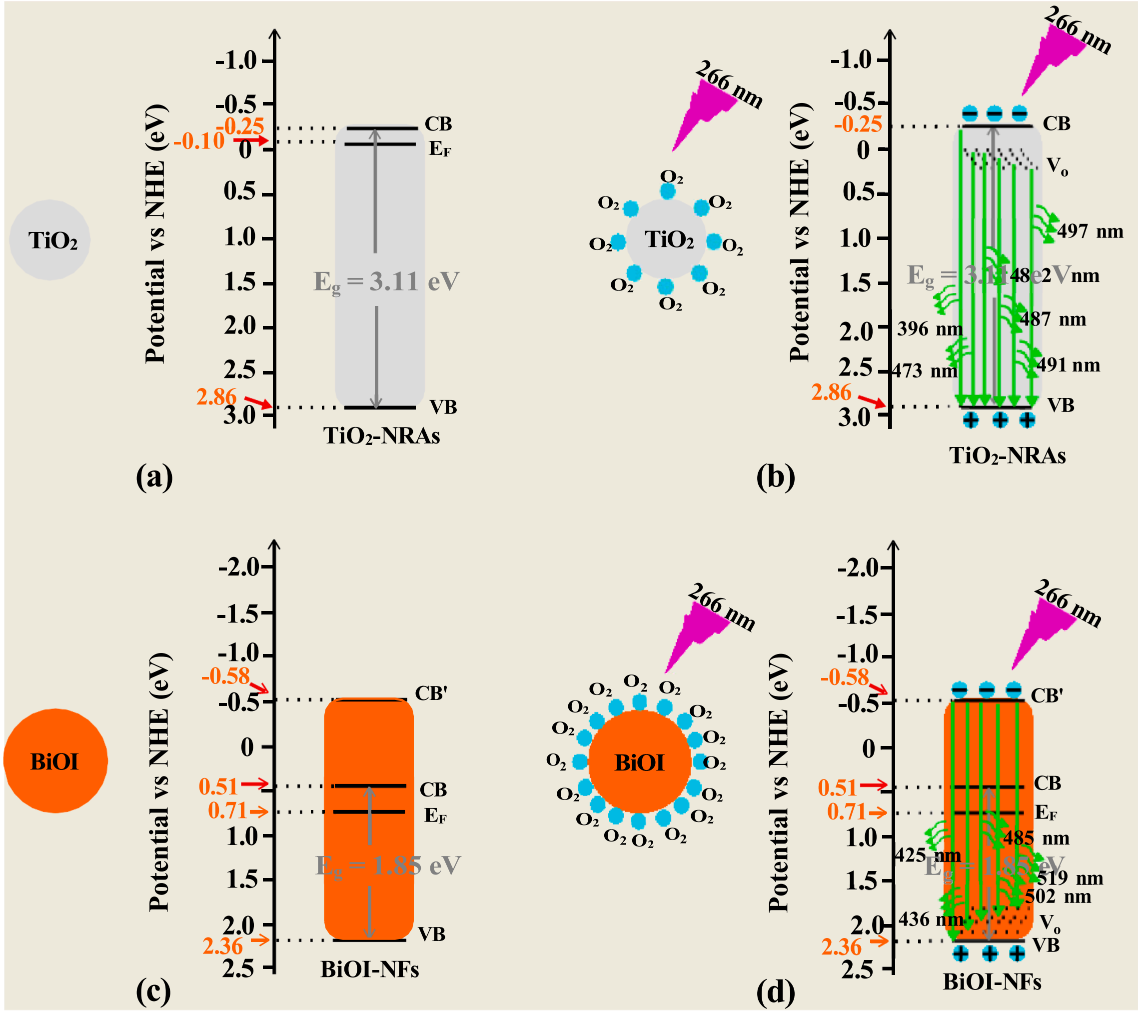

**Figure 8.** (a)-(d) Diagrammatic sketchs of (a, c) are CB, VB, and $E_F$ potential positions (vs. NHE) for single $TiO_2$-NRAs and BiOI-NFs films before photo-irradiation conditions, respectively; Schematic diagrams (b, d) are photogenerated carriers generated, transferred, and recombination for pristine $TiO_2$-NRAs and pure BiOI-NFs films in atmosphere irradiated by UVC light, severally.

5.94 eV, (Shilpa et al., 2023; Ju et al., 2023) respectively. $E_e$ was the energy of free electrons on the hydrogen scale (~4.5 eV vs.

$E_{NHE}$). Consequentially, $E_{VB}$ and $E_{CB}$ of $TiO_2$-NRAs are estimated to be 2.86 eV and -0.25 eV vs. NHE, and those of BiOI-NFs are 2.36 eV and 0.51 eV vs. NHE respectively, which agrees with the previous reports. (Shao et al., 2022; Wang et al., 2022) Additionally, it should be noted that the $E_F$ values of $TiO_2$ and BiOI as reported severally are -0.10 eV and 0.71 eV vs. NHE, and are depicted in Figures 8(a) and 8(c). In Figures 8 (b) and 8(d), we illustrated the processes of the generation, transfer, and radiative recombination of the photoexcited charge carriers in the $TiO_2$-NRAs alone and pristine BiOI-NFs when exposed to 266 nm light. Simultaneously, oxygen molecules ($O_2$) have a tendency to attach on the surfaces of individual $TiO_2$-NRAs and alone BiOI-NFs without external assistance. For the specimen of undecorated $TiO_2$-NRAs (Figure 8(b)), the large number of electrons in the VB were excited to the CB by the incident photon energy, leaving behind holes in the VB of $TiO_2$-NTAs. This occurs when the photon energy (4.7 eV) is greater than the value of $E_g$ (3.11 eV) of $TiO_2$-NRAs. At the initial stages of UVC photoexcitation ranged as 0 ns – 1.5 ns, the concentration of the $e^-$ in the CB of TiO achieved the maximum value because there was no more generation of charges until the next cycle of light irradiation. We detected three transient PL profiles sited at 396 nm, 491 nm, and 497 nm, which could be ascribed to the NBE direct radiative recombination of photogenerated $e^-$ - $h^+$ pairs and indirect radiative transitions between $V_o$ defects and $h^+_{VB}$ in $TiO_2$ respectively, as illustrated in Figure 7(a). Based on previously investigated, we are more inclined to believe that free electrons in CB of semiconductor will preferentially transition to adjacent $V_o$ defects rather than holes in VB and deep-trapping defect levels. (Zhou et al., 2023) Meanwhile, the $V_o$ defect energy levels consist of a series of discrete levels that act as shallow donor levels slightly below the CB of anatase $TiO_2$. (Zhang et al., 2022) Thus, it can be logically believed that the transient PL profiles centered at 487 nm, 482 nm, and 473 nm gradually decreased with the recording time from 3 ns to 6 ns, originating from the indirect radiative recombination between $V_o$ defects and $h^+_{VB}$, which was accompanied by a blueshift of the transient PL peaks. When the sole BiOI-NFs nano-semiconductor irradiated by 266 nm light, the transient process of photo-excited charge carriers generated, transferred, and radiative recombination as schematically illustrated in Figure 8(d). Apparently, plenty of electrons in the VB are promoted across the forbidden band to the CB (0.51 eV vs. $E_{NHE}$), remaining holes in the VB of BiOI; it is worth emphasizing that the $e^-_{CB}$ in BiOI could be elevated to higher energy level (denoted as CB$'$) when triggered by UVC light would reach -0.58 eV. (Yosefi and Haghighi, 2018) In the initial-time of UVC photoexcitation (t = 0 ns), the amount of photogenerated carriers in BiOI-NFs should be achieved the minimum value until transiently terminated for the 266-nm light irradiation. Coinstantaneously, the photo-triggered electrons in CB$'$ ($e^-$) could be recombined with the V defects resulting in transient radiative PL transition, which benefitted

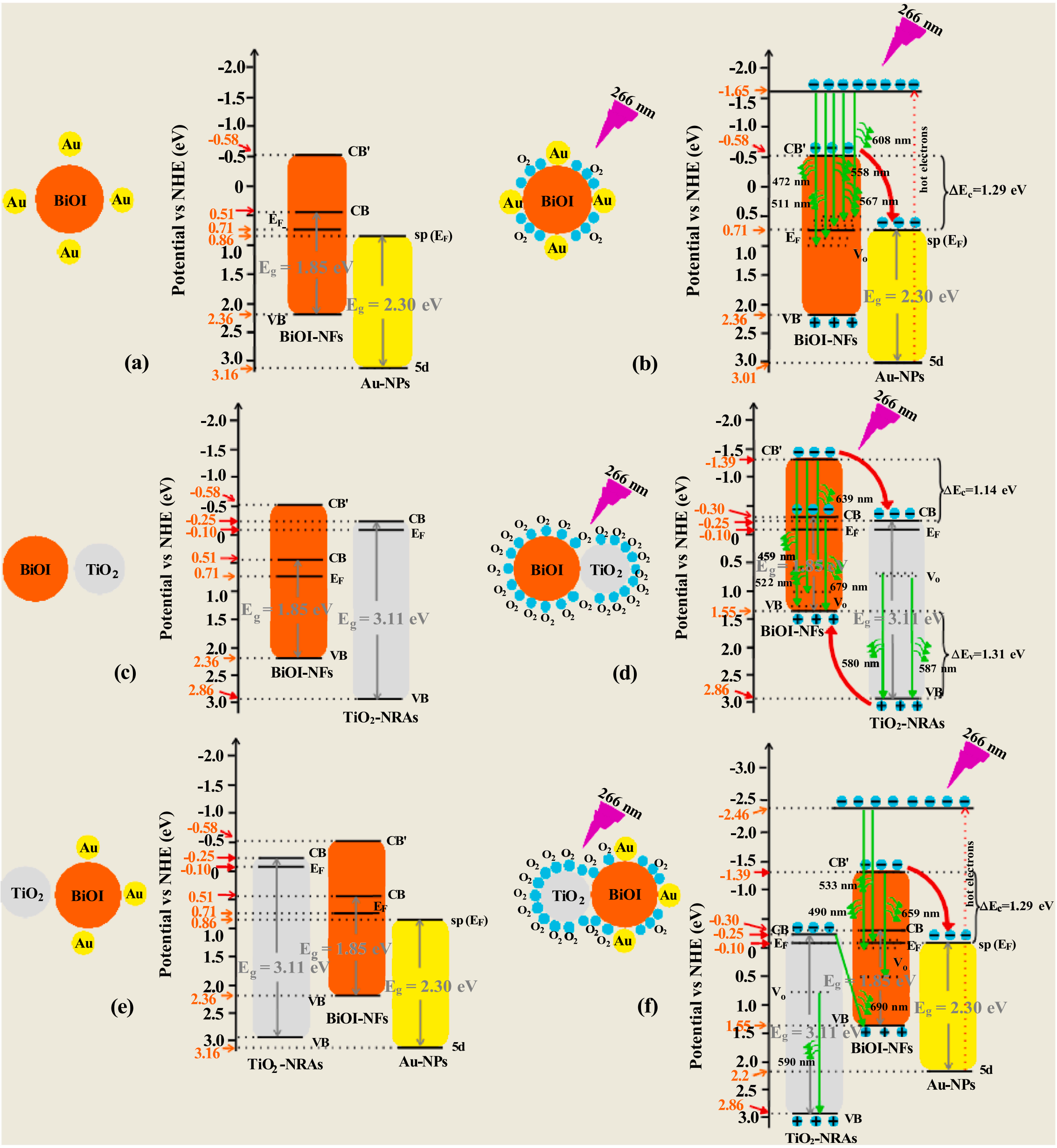

**Figure 9.** (a)-(f) Diagrammatic sketchs of (a, c, e) CB, VB, and $E_F$ potential positions (vs. NHE) for individual $TiO_2$-NRAs, BiOI-NFs, and Au-NPs before contact; (b, d, f) are band-gap structure, charge carriers photoexcited and transient charge transfer behaviors for BiOI-NFs/Au-NPs, $TiO_2$-NRAs/BiOI-NFs, and $TiO_2$-NRAs/BiOI-NFs/Au-NPs nanohybrids after irradiated by UVC light, respectively.

from the $V_o$ defects could serve as photoexcited holes trapping centers to ameliorate the charge separation and transmission. (Fu et al., 2021) As we observed, the transient PL peaks located at 519 nm appeared, resulting from $e^-$ spontaneously preferentially transition to the neighboring V defects compared with VB directly radiative recombination. (Zhou et al., 2023) Furthermore, the $e^-$ were inclined to transition to more deeper $V_o$ defect levels as the concentrations of them gradually increased. Conceivably, transient PL emission peaks sited at 502 nm, 485 nm, and 436 nm appeared in succession with the evolution of recording time from 1.5 ns to 4.5 ns. At the final moment of spectral recording (t =ns), a transient PL peak located at 425 nm, which can be attributed to directly radiative recombination between $e^-$ - $h^+$ , consistenting with the calculated E values of BiOI-NFs.

In order to further evaluated the essence of Au-NPs mediated interfacial CT behaviors between the interface of BiOI-NFs and $TiO_2$-NRAs, we now present two plausible electron transfer scenarios, including conventional type-II and Z-scheme CT routes mediated by Au-NPs, the detailed schematic illustrations are shown in Figures 9(a)-(f). We present the potential energy positions of the CB', CB, VB, and $E_F$ for the BiOI-NFs against NHE without light irradiation in Figure 9(a). These specific potential energy values for BiOI-NFs are consistent with the Figure 8(c) previously presented. Building upon previous research findings, (Fu et al., 2019) Au-NPs has an sp-band that spans the $E_F$ and exhibits a dispersion pattern similar to that of free electrons. As a result, plasmonic excitations in Au-NPs essentially involve intraband electronic transitions that occur within the sp-band. That is, interband transitions lead to the excitation of electrons from filled d-bands to empty states within the sp-band. The potential energy locations of sp-band (i.e., $E_F$) and d-band are 0.86 eV and 3.16 eV (vs. $E_{NHE}$), hinting electron in d-band is around 2.3 eV below the site of $E_F$, as the schematic illustration of band gap structure of sole Au-NPs presents in Figure 9(a). Figure 9(b) presented the band-gap structure information of the BiOI-NFs/Au-NPs integrated M-S nano-heterostructures aerated in an atmosphere with 266-nm light irradiation, while the $O_2$ molecules could be much efficiently adsorbed on the surface $V_o$ defects of BiOI-NFs instantaneously. Initially, the BiOI-NFs and Au-NPs are in contact with each other without light irradiation, the electrons naturally transferred from BiOI to Au, owing to the difference in the $E_F$ values between of them as stated above. Consequently, the formation of CB offset ($\Delta E_c$) of BiOI-NFs/Au-NPs heterojunction is entirely reasonable, which was equal to 1.14 eV, resulting from the alignment of their $E_F$ levels. In the initial UVC photoexcitation toward BiOI-NFs/Au-NPs (t = 0 ns), plenty of electrons in the VB are promoted to the CB' of BiOI to generate $e^-_{CB'}$, remaining holes in the VB to produce $h^+_{VB}$, owing to the incident photon energy is more greater than the $E_g$ value of BiOI-NFs. Almost simultaneously, the $e^-$ in BiOI are driven by the force of BEF and transferred to the sp-band of Au-NPs in a favorable manner; while the electrons in the 5d-band of Au-NPs are rapidly excited to higher energy levels (located at -1.65 eV vs. $E_{NHE}$) by the irradiation of 266-nm light, and are referred to as "hot electrons". (Fu et al., 2019) At the initial moment of spectral recording, (i.e., t = 0 ns) a transient PL profile located at 608 nm was observed, which originated from the radiative recombination relaxation process between the hot electrons and $V_o$ defects. As the spectral recording time evolutions from 1.5 ns to 6 ns, more $e^-$ are injected from the CB' of BiOI-NFs into the sp-band of Au-NPs driven by ΔE , and then a large number of electrons in the 5d-band of Au-NPs are pumped to higher energy levels triggered by plasmons effect and become hot electrons. Thus, the transient PL peaks sites at 567 nm, 558 nm, 511 nm, and 472 nm appeared successively at different recording points with an interval of 1.5 ns, accompanied by the increasing concentration of hot electrons. They are likely due to the interaction of hot electrons with deeper $V_o$ defects in BiOI-NFs, resulting in radiative recombination. Subsequently, as schematically illustrated in Figure 9(c)-(d), we demonstrated a conceivable mechanism of the interfacial CT avenue towards BiOI-NFs/$TiO_2$-NRAs binary nanoheterojunctions irradiated by 266-nm fs light, aiming to elucidate the above NTRT-PL emission (Figure 7(d)). It is comprehensible that there is no CT process before sole BiOI-NFs and isolated $TiO_2$-NRAs contact, accompanying with atmospheric $O_2$ molecular that was adsorbed on the surface of the BiOI-NFs and the $TiO_2$-NRAs, respectively. Consequently, the surface energy bands of them are rather flat. The $E_g$ values of BiOI and $TiO_2$ severally are 1.85 eV and 3.11 eV, and their $E_F$ positions sited at 0.71 eV and -0.10 eV (vs. $E_{NHE}$), respectively. In the case of the BiOI-NFs and $TiO_2$-NRAs semiconductors are in intimate contact without light irradiation, a BiOI-NFs/$TiO_2$-NRAs integrated nano-heterostructure potential barrier is formed at the interface between the BiOI-NFs and $TiO_2$-NRAs, resulting from the alignment of their different $E_F$ positions as stated above, which provoked the energy difference values ($ED_v$) between BiOI and $TiO_2$, that is, the calculated $\Delta E_c$ is 1.14 eV, and the $ED_v$ of the VB (i.e., the VB offset, $\Delta E_v$) equal to 1.31 eV, as schematically illustrated in Figure 9(d). In the circumstances of the BiOI-NFs/$TiO_2$-NRAs nano-heterojunctions irradiated by 266 nm light, the schematic diagrams of detailed NTRT-PL spectra and the plausible type-II CT process for binary nanohybrids are presented in Figures 7(d) and 9(d), respectively. In the initial UVC photoexcitation (t = 0 ns), plenty of electrons in the VB are promoted across the forbidden gap to the CB to produce $e^-$ , remaining holes in the VB to create $h^+$ ; Of particular note is that, for the BiOI-NFs, not only can its electrons in the VB be excited into the CB, but also into metastable states (i.e., CB') at energy levels higher than the CB, benefitting from the incident photon energy that is greater than the energy difference between the excited state and the VB. Furthermore, the observation of the transient PL profile at a wavelength of 679 nm is easily comprehensible, as its emission originates from the direct radiative recombination of $e^-$ - $h^+$ pairs of BiOI. With the increased spectral recording time (t = 1.5 ns), photogenerated carriers in CB' of BiOI driven by the BEF, the $\Delta E_c$ (i.e., 1.14 eV) can supply the intrinsic driving force for photogenerated $e^-$ migrating from the CB' of BiOI to the CB of TiO , while the ΔE (i.e., 1.31 eV) could promote the photoexcited $h^+_{VB}$ transfer from the VB of $TiO_2$ to the VB of BiOI in the opposite direction, which directly witnessed the conventional type-II CT route. So, we observed that two transient PL emission peaks located at 587 nm and 639 nm in the NTRT-PL spectrum, which attributed to $V_o$ trapping states of $TiO_2$ radiative transition with the $h^+_{VB}$ and photogenerated $e^-$ in BiOI radiative recombination with V defects. As the recording of transient spectra evolves over time (t = 3 ns), we are increasingly inclined to believe that the transient emission peak at 580 nm is due to the radiative relaxation between $V_o$ defects and $h^+_{VB}$ in $TiO_2$. With the concentration of $e^-$ for BiOI-NFs increasing when the recording time was increased from 4.5 eV to 6 eV, naturally causing the peak position of the transient spectrum to blue-shift from 522 nm to 459 nm. This shift is rooted in the radiative transition between photoexcited carriers $e^-$ and V defects. To deepen understanding of the variation of transient PL peak versus recording time evolution for $TiO_2$-NRAs/BiOI-NFs/Au-NPs nano-heterojunctions in atmospheric environment irradiated by 266-nm light, we proposed the persuasive –Z-scheme‖ interfacial CT channel among ternary nano-heterostructures mediated by Au-NPs. Figure 9(e) shows the essential potential energy positions against $E_{NHE}$ for pristine BiOI-NFs, separate $TiO_2$-NRAs, and isolated Au-NPs without light irradiation, the specific potential energy positions of CB, VB, 5d, sp, and $E_F$ of them are consistent with the above stated. Figure 9(f) exhibits the adjusted potential energy position of band structure for integrated $TiO_2$-NRAs/BiOI-NFs/Au-NPs nanohybrids aerated in an atmosphere at dark condition. Spontaneously, $O_2$ molecules could be adsorbed on the surface of nanocomposites. It is plausible to believe that a staggered nanoheterojunction barrier is established in the interfacial region of the BiOI-NFs and Au-NPs, which is triggered by the alignment of their different $E_F$ potential positions as stated above. Consequently, the value of $\Delta E_c$ between BiOI and Au was calculated to be 1.29 eV. When the nano-heterojunction composites was irradiated by fs-light with a wavelength of 266 nm, the electrons in the VB of the BiOI-NFs and $TiO_2$-NRAs were inevitably excited to the CB' and CB with simultaneous survived holes in the VB, owing to the fact that the radiated photon energy was larger than both the $E_g$ values of the BiOI-NFs and $TiO_2$-NRAs. Synchronously, the energy of incident photons can excite electrons in the 5d-band located in Au-NPs to higher energy levels (ca. -2.46 eV), transforming them into hot electrons. In the prime of UVC light irradiation (t = 0 ns), the photo-excited free carriers in the CB' of BiOI-NFs are autonomously transferred to the sp-band of Au-NPs under the driving force of $\Delta E_c$, leading to a sharp decrease in the concentration of free carriers in the CB'. A transient PL peak with a wavelength of 690 nm is detected instantly, and we inclined to believe that the transitory peak can be attributed to the –Z-scheme‖ radiative recombination of the $e^-$ in CB of TiO -NRAs and the $h^+_{VB}$ in VB of BiOI-NFs. (Zhang et al., 2022) The concentration of the $e^-$ of BiOI-NFs increasing when the irradiation time was increased from 0 ns to 1.5 ns, the new transient radiative PL peak emerged at 659 nm, originating from the indirect radiative PL recombination between the $e^-$ in CB' of BiOI and the $V_o$ trapping defects. Analogously, the concentration of $e^-$ in TiO increased with the evolution of recording time (t = 3 ns), the transient PL peak located at 590 nm, which could be ascribed to the radiative transition between the $V_o$ defects and the VB of $TiO_2$-NFs. Afterwards, the concentration of the $e^-$ in BiOI decreased with the evolution of the spectral recording time from 4.5 ns to 6 ns, the plasmonics effect provide a facilitated manner for the hot electrons injection from the Au-NPs to the BiOI-NFs, resulting in the boosted transient PL profiles of the emitted wavelengths sited at 533 nm and 490 nm, which were rooted from the radiating transition related with $V_o$ defects in BiOI-NFs.

The PEC activities and bioanalysis performances of a semiconductor nanoheterostructure has a positive correlation with the lifetime of charge carriers. Therefore, a comparison of carrier lifetime in heterostructure and single semiconductor can yield useful information about these material's charge-separation behaviour. The NTRT-PL and TRPL techniques have contributed significantly to our understanding of photoinduced charge carrier dynamics at the interfaces between different semiconductors. The TRPL measurement is a powerful analytic tool and allows us to inspect the kinetics of excited state by monitoring the emissive transitions on the component of interest. Figure S2 (SI) exhibits the typical PL decay profiles recorded by repetitively exciting the as-prepared specimens with 375 nm laser pulses. And these PL decay traces were collected at 396 nm, 425 nm, 608 nm, 639 nm, and 659 nm, for the specimens of single semiconductor, binary and ternary nano-heterostructures. The emission peaks sited at 396 nm and 425 nm can be attributed to the direct radiative recombination of individual semiconductors $TiO_2$-NRAs and BiOI-NFs, respectively. Other PL peaks can be attributed to the indirect radiative recombination of $V_o$ defects in binary and ternary nano-heterostructures of BiOI-NFs. The TRPL decay curves showed a non-single exponential feature and can be mathematically described as the following biexponential function: $I(t) = A_1exp(-t/\tau_1) + A_2exp(-t/\tau_2)$, where $\tau_1$ and $\tau_2$ are the lifetime of the different components, $A_1$ and $A_2$ are the contribution ratio of each component to the total decay. As compared to separated $TiO_2$-NRAs and individual BiOI-NFs, the others three heterostructure nanohybrids displayed prolonged PL decay kinetics characteristic of pronounced charge separation. For global comparison, the intensity-weighted average lifetime ($\tau_{avg}$) was computed by the expression $\tau_{avg} = (A_1 \tau_1^2 + A_2 \tau_2^2)/(A_1 \tau_1 + A_2 \tau_2)$. As tabulated in Table S3 (SI), the longer lifetime $\tau_1$ is attributed to the inter-band recombination of the photo-induced excitons, which mainly contributes to the PL; and the shorter lifetime $\tau_2$ is related to the non-radiative relaxation. Simultaneously, the calculated

$\tau_{avg}$ values of pristine $TiO_2$-NRAs, pure BiOI-NFs, BiOI-NFs/Au-NPs, and $TiO_2$-NRAs/BiOI-NFs were 3.25 ns, 3.27 ns, 3.32 ns, and 3.65 ns, respectively. Conspicuously, the $\tau_{avg}$ value of ternary $TiO_2$-NRAs/BiOI-NFs/Au-NPs nanoheterostructures is prolonged to 4.16 ns, suggesting the high efficacy of the Z-scheme nanoheterojunctions.

As we known, PL quantum yield (PLQY,η) could be evaluated as the fraction of radiative recombination among all the recombination processes of the charge carrier as : $\eta = (\Sigma_i A_i k_{rad}^i)/(\Sigma_i A_i k_{rad}^i + \Sigma_j A_j k_{nonrad}^i +)$ (i.e., $1/\tau_2$) are the rates of the radiative and nonradiative recombination recombination processes, (Huang et al., 2011) respectively, and $A_{i,j}$ represents the amplitude of each decay component. As itemized in Table S3 (SI), the PLQY for the specimens of pristine $TiO_2$-NRAs, pure BiOI-NFs, BiOI-NFs/Au-NPs, $TiO_2$-NRAs/BiOI-NFs, and $TiO_2$-NRAs/BiOI-NFs/Au-NPs were 4.3%, 4.9%, 5.8%, 8.9%, and 9.9%, respectively. Notably, the $TiO_2$-NRAs/BiOI-NFs/Au-NPs sample exhibits the highest PLQY value. Specifically, the photo-induced electrons in the CB of $TiO_2$-NRAs can efficiently annihilate the holes in the VB of BiOI-NFs, thus suppressing the recombination of photo-induced excitons inside each component. As a consequence, more photo-induced electrons would be preserved on the CB of BiOI-NFs, and more photo-induced holes would be preserved on the VB of $TiO_2$-NRAs, thus leading to superior PLQY characteristic and enhanced PEC performances. Furthermore, the incorporation of Au-NPs also results in prolonged average lifetimes with significantly altered $\tau_1$ and $\tau_2$. The dispersed Au-NPs not only act as effective trap sites to capture the photo-induced electrons from the CB' of BiOI-NFs, but also serve as –charging storage‖ to inject the high-energy hot electrons into the CB' of BiOI-NFs, thereby increasing the concentrations of $e^-$ in BiOI-NFs. Therefore, for ternary $TiO_2$-NRAs/BiOI-NFs/Au-NPs nanoheterohybrids, the Z-scheme CT process and the decorated Au-NPs synergistic contribute to the efficient separation of the photo-induced excitons.

The textural properties of the binary and ternary heterostructure nanohybrids were characterized using $N_2$ adsorption-desorption experiments, and the results are depicted in Figure S3 (SI). And the textural parameters (including BET surface area ($S_{BET}$) and pore volumes ($V_p$)) calculated based on the isotherms for the as-prepared heterostructure nanohybrids are tabulated in Table S4 (SI). Apparently, the specimen of pure BiOI-NFs do not belong to the mesoporous characteristics with values of $S_{BET}$ and $V_p$ are 9.8 $m^2/g$ and 0.02 $cm^3/g$, proving that the BiOI-NFs sample is dense and non-porous, which probably ascribed to the aggregation of BiOI nanoflakes. Simultaneously, we distinctly observed that the BiOI-NFs/Au-NPs sample has a larger specific surface area compared to the individual BiOI-NFs nanosystems with values of $S_{BET}$ and $V_p$ are 15.5 $m^2/g$ and 0.03 $cm^3/g$ respectively, benefitting from the deposition of Au-NPs, which could promoted the adsorption performances of the nanocomposites. (Guan et al., 2022) Furthermore, it is evident that the relative pressure ($P/P_0$) of the loop tends to 1 for the specimens of pristine $TiO_2$-NRAs, $TiO_2$-NRAs/BiOI-NFs, and $TiO_2$-NRAs/BiOI-NFs/Au-NPs, which indicate the presence of mesopores and it can be classified as type IV according to the International Union for Pure and Applied Chemistry (IUPAC) standard. From the SEM images of Figure 1, it can be seen that the prepared $TiO_2$-NRAs has finer pores presumably arise from the intra-aggregation of nanorods array of $TiO_2$, and the edge of the $TiO_2$-NRAs/BiOI-NFs is covered with flake-like nanoflower BiOI. Additionally, the broader pores distributed in $TiO_2$-NRAs/BiOI-NFs/Au-NPs could be attributed to inter-aggregation between $TiO_2$-NRAs, and BiOI-NFs/Au-NPs. As listed in Table S4 (SI), it is found that pristine $TiO_2$-NRAs has a less $S_{BET}$ value of 22.8 $m^2/g$, while the values of $S_{BET}$ for $TiO_2$-NRAs/BiOI-NFs, and $TiO_2$-NRAs/BiOI-NFs/Au-NPs specimens are 28.7 $m^2/g$, and 37.9 $m^2/g$ respectively, which coincided with the results of SEM images. Besides, the values of $V_p$ for pristine $TiO_2$-NRAs, $TiO_2$-NRAs/BiOI-NFs, and $TiO_2$-NRAs/BiOI-NFs/Au-NPs are 0.06 $cm^3/g$, 0.13 $cm^3/g$, and 0.18 $cm^3/g$, which of them increased with the successive deposition of BiOI-NFs and Au-NPs in the $TiO_2$-NFs.

The electrochemical double-layer capacitance ($C_{dl}$) method was used to evaluate the electrochemically active surface area (ECSA) of as-prepared hetero-nanohybrids, which can be calculated by CV tests at different scan rates increasing from 20 mV/s to 100 mV/s (Figure S4 (a)-(e) (SI)). The NHE electrode was calibrated with relative to RHE: $E_{(RHE)} = E_{(NHE)} + 0.059 \times pH$. The slopes of the plots were used to express double the $C_{dl}$ values, as plotted in Figure S4(f) (SI). As summarized in Table S4 (SI), the $C_{dl}$ values of pristine $TiO_2$-NRAs, pure BiOI-NFs, BiOI-NFs/Au-NPs, $TiO_2$-NRAs/BiOI-NFs, and $TiO_2$-NRAs/BiOI-NFs/Au-NPs were 10.27 μF $cm^{-2}$, 43.31 μF $cm^{-2}$, 71.19 μF $cm^{-2}$, 87.92 μF $cm^{-2}$, and 96.36 μF $cm^{-2}$, respectively. The BiOI-NFs/Au-NPs photoelectrode possessed more active surface reactive sites than pure BiOI-NFs sample, which further confirms that the proper loading of Au-NPs was of significant importance because it probably enlarged the nano-heterojunctions specific surface area and then affected the surface reaction. The larger $C_{dl}$ value is likely to promote carrier transfer and probably enhance PEC performance. On the contrary, the pure BiOI-NFs sample with a poor ECSA response can be explained by the reason that the BiOI aggregates with a flower-like flake structure reduced effective heterojunction interface areas between $TiO_2$-NRAs and BiOI-NFs, extremely likely resulting in fewer adsorption active centers in the PEC process. Besides, these findings suggest that compared with the pristine $TiO_2$-NRAs, the higher values of $S_{BET}$ and $C_{dl}$ for the $TiO_2$-NRAs/BiOI-NFs, and $TiO_2$-NRAs/BiOI-NFs/Au-NPs would probably be facilitated to elevate the PEC performance, which could be attributed to the synergistic effect of decoration of BiOI-NFs and Au-NPs.

In order to further explore the synergistic impact of Au-NPs decoration and surface vacancies states on the charge separation, migration, and recombination of photoinduced $e^-$ - $h^+$ pairs at the heterointerfaces between the BiOI-NFs and $TiO_2$-NRAs, the transient photocurrent response and EIS characteristics were performed to reveal the mobility and transfer dynamics of photoexcited carriers, which are closely associated with the PEC performance. We observed the photoresponse switching behavior of the product during eight successive photo-switching cycles at an interval of 20s, illustrating that the as-prepared specimens could produce carriers under simulated solar light irradiation, which can reflected the surface enrichment degree of photo-generated charges. It can be noted from Figure S5(a) (SI)that the order of the instantaneous photocurrent density of as-obtained specimens is: $TiO_2$-NRAs/BiOI-NFs/Au-NPs > $TiO_2$-NRAs/BiOI-NFs > BiOI-NFs/Au-NPs > pure BiOI-NFs > pristine $TiO_2$-NRAs. It is not surprising to observe that the smallest photocurrent value (ca. 1.15 μA/$cm^2$) for pristine $TiO_2$-NRAs, which could be ascribed to its wider $E_g$ value obstructed the light absorption expand to longer wavelength; while the original BiOI-NFs revealed a higher photocurrent response (ca. 1.43 μA/cm$^2$) than that of pure $TiO_2$-NRAs, with the on/off switch benefiting from the reduced value of $E_g$ that corresponds to greater light absorption ranges. The BiOI-NFs/Au-NPs and $TiO_2$-NRAs/BiOI-NFs binary hetero-nanohybrids exhibited more sensitive photocurrent responses (i.e., ca. 2.61 μA/cm$^2$ and ca. 3.27 μA/cm$^2$) compared with the single semiconductor, suggesting that the introduction of Au-NPs and the construction of type-II nanoheterojunctions could effectively accelerate the separation and transfer of photoinduced $e^-$ - $h^+$ pairs. Strikingly, the $TiO_2$-NRAs/BiOI-NFs/Au-NPs specimen demonstrated the highest photocurrent density value (ca. 3.86 μA/cm$^2$), hinting the ternary nanohybridization possesses strongest ability of producing $e^-$ - $h^+$ pairs and prolonging the lifetime of photogenerated carriers, which most probably be attributed to the synergistic effect of plasmon injection induced by Au-NPs and facilitated charge separation mediated by intrinsic defects.

To delve deeper into the nature of the prepared nanomaterials and illuminate the intrinsic connection between the transfer and recombination of charge carriers, EIS was employed to delve into the gradual assembly of the PEC performance, which heavily relies on its remarkable ability to assess the interfacial CT and the separation process occurring between the electrode and the electrolyte solution. As depicted in Figure S5(b) (SI), it is customary for the Nyquist plot obtained from an EIS measurement to manifest as a captivating series of semicircular arcs at higher frequencies, complemented by a linear segment at lower frequencies. The semicircle in the high-frequency region was related to the impedance of CT, and the larger diameter of the semicircle, the greater the impedance. The semicircular diameters of the specimens display a hierarchical arrangement as follows: $TiO_2$-NRAs/BiOI-NFs/Au-NPs < $TiO_2$-NRAs/BiOI-NFs < BiOI-NFs/Au-NPs < pure BiOI-NFs < pristine $TiO_2$-NRAs. This observation presents a strikingly opposite ranking compared to the order displayed by the transient photocurrent response mentioned earlier. The pronounced observation reveals that the diameter of the original $TiO_2$-NRAs is the largest, likely attributed to the inadequate responsiveness of $TiO_2$ to long-wavelength light, consequently impeding the rate of electron conduction. While the impedance arc radius of unaltered BiOI-NFs emerged the smaller than that of original $TiO_2$-NRAs, implying the much lower charge transportation resistance and more photogenerated $e^-$ - $h^+$ pairs generation for BiOI-NFs. As excepted, the BiOI-NFs/Au-NPs and $TiO_2$-NRAs/BiOI-NFs samples exhibited smaller CT resistance values compared with any other separated semiconductors, indicating that binary nano-heterojunctions were advantageous in promoting charge separation efficiency and accelerating transport of electrons. It is noteworthy that the ternary $TiO_2$-NRAs/BiOI-NFs/Au-NPs nanohybrids has the smallest impedance arc radius, exhibiting the lowest interfacial CT resistance and highest migration efficiency of photoinduced carriers, which can be attributed to the synergistic effect of elevated carriers amounts induced by plasmons and facilitated electrons transport supported by intrinsic defects. This reveals that the rational construction of $TiO_2$-NRAs/BiOI-NFs/Au-NPs ternary nanoheterostructures by introducing proper amounts of Au-NPs to binary $TiO_2$-NRAs/BiOI-NFs nanohybrids can greatly improve the separation efficiency of photo-generated $e^-$ - $h^+$ pairs in the resulting PEC performances.

With the aim of obtaining a more encompassing exploration of the CT pathway and confirming the contrasting abundance of surface vacancies defects within binary and ternary nanohetero-hybrids, ESR analysis was conducted using DMPO as the trapping agent to investigate the amount of $\bullet O_2^-$ and •OH radicals in both illumination and dark conditions, which provided the most compelling evidence for detecting reactive species, and the results were demonstrated in Figure S6(a)-(d) (SI). As shown in Figures S6(b) and (d) (SI), no obvious DMPO-$\bullet O_2^-$ and DMPO-•OH characteristic signals are observed for as-obtained specimens in the darkness, proving that no active species were generated. While under simulated solar light irradiation for 10 minutes, the signal peaks of DMPO-$\bullet O_2^-$ adducts exhibited clear quartet wave signals with peak intensity ratios indicated by 1:1:1:1 split peaks in all as-prepared samples, indicating the emergence of $O_2^-$ radical in nano-system, which was illustrated in Figure S6(a) (SI). Analogously, as exhibited in Figure S6(c) (SI), the intensity ratio of the apparent quartet was 1:2:2:1, assigning to DMPO-•OH adducts, which indicated that the •OH radicals were explicitly detected. Simultaneously, it is clear that the peaks intensity of the DMPO-$\bullet O_2^-$ adduct for the as-obtained specimens is as follows: $TiO_2$-NRAs/BiOI-NFs/Au-NPs > $TiO_2$-NRAs/BiOI-NFs > BiOI-NFs/Au-NPs > pure BiOI-NFs > pristine $TiO_2$-NRAs, and the result is in accordance with the rank of characteristic peaks intensity of DMPO-•OH. Apparently, a weak DMPO-$\bullet O_2^-$ signal was detected in pristine $TiO_2$-NRAs due to its CB position (-0.25 eV vs. $E_{NHE}$) close to the reduction potential of $O_2/\bullet O_2^-$ (-0.33 eV vs. $E_{NHE}$). (Shao et al., 2023) Compared with pristine $TiO_2$-NRAs, the characteristic peak intensity of DMPO-$\bullet O_2^-$ adduct in pure BiOI-NFs is slightly higher than that of $TiO_2$-NRAs. This can be entirely attributed to the higher CB reduction potential (-0.58 eV vs. NHE) of pure BiOI-NFs compared to that of $TiO_2$-NRAs. Furthermore, the DMPO-$\bullet O_2^-$ signal intensity of the binary nanoheterostructures is higher than that of original semiconductors, it can be concluded that the increased efficiency of photogenerated charge separation and migration due to the electron transfer driven by powerful force of built-in field makes the binary nanoheterojunctions have more efficient reducing electrons, proving that the CT mechanism is conventional type-II heterojunctions. It is worth noting that the ESR signal intensities of both $\bullet O_2^-$ and •OH groups for $TiO_2$-NRAs/BiOI-NFs is stronger than that of BiOI-NFs/Au-NPs. Clearly, this can be attributed to the higher CB reduction potential value (-1.39 eV vs. $E_{NHE}$) of the $TiO_2$-NRAs/BiOI-NFs, surpassing the potential value (-0.58 eV vs. $E_{NHE}$) of CB in BiOI/Au-NPs, which results in the generation of a higher concentration of active $\bullet O_2^-$ groups. Based on the following reaction equation, $\bullet O_2^- + 2H_2O \rightarrow H_2O_2 + \bullet OH + OH^-$, it is evidently observed that a higher concentration of $\bullet O_2^-$ inevitably leads to the generation of a greater amount of •OH groups. Hence, it is clear that the ESR characteristic peak intensities of both $\bullet O_2^-$ and •OH groups for the binary $TiO_2$-NRAs/BiOI-NFs and BiOI/Au-NPs nanoheterostructures exhibited the same trend of variation.

Strikingly, the intensities of DMPO-$\bullet O_2^-$ and DMPO-•OH signals for $TiO_2$-NRAs/BiOI-NFs/Au-NPs ternary nanohetero-hybrids are significantly higher than that of others crafted specimens, suggesting that highest quantity of $\bullet O_2^-$ and •OH radicals can be generated during the photo-irradiation process. The reasons can be primarily attributed to the following three factors: (i) the LSPR effect induces a significant injection of "hot-electrons" from Au-NPs into the adjacent CB of BiOI-NFs, facilitating abundant generation of $e^-$ ; (ii) the deposition of Au-NPs and the presence of numerous $V_o$ defects in the ternary nanoheterostructures could act as active sites for the surface adsorption of $O_2$; (iii) the synergistic effect of a higher oxidation-reduction potential and the Z-scheme CT mechanism provides a facilitated and efficient pathway for the high concentration of $e^-$ to capture adsorbed O and generate $\bullet O_2^-$ (•OH) radicals, facilitated by forceful built-in field.

We conducted photodegradation tests of the as-obtained hetero-nanohybrids to testify to the feasibility of the as-proposed transient Z-scheme CT channels, combining with the synergistic effect between Au-NPs plasmon and substantial intrinsic $V_o$ defects.

The photodegradation performance of binary and ternary heterostructure nano-systems was assessed under standard simulated solar spectrum irradiation, using a 15 mg/L MO solution as the target. To eliminate the possibility of photobleaching by MO, a control experiment was conducted by exposing a blank MO dye solution to UV-Visible light without the presence of a catalyst. This was done to confirm that the observed photodecomposition of MO was indeed attributed to the catalyst. Once the adsorption-desorption equilibrium of the dye on the specimen was achieved, the photocatalytic nanoheterostructure was mixed with the MO aqueous solution and stirred in the dark for 1 h. Prior to initiating the photocatalysis reaction, the maximum adsorption of MO on the nanohybrids was determined by recording the UV-Vis absorption spectra.

The calibration curve was constructed using MO dye solutions at various concentrations (8 mg/L, 10 mg/L, 15 mg/L, 20 mg/L, 25 mg/L, 30 mg/L) plotted against the corresponding absorbance values at the maximum wavelength of 464 nm. As shown in Figure 10, the linear regression equation yielded a correlation coefficient ($R^2$) of 0.9986, indicating an excellent fit of the curve. Within the concentration range below 30 mg/L, the relationship between solution concentration and absorbance follows the Lambert-Beer Law, exhibiting a linear behavior. The high degree of fitting is evident, allowing for the straightforward calculation of MO solution concentration by measuring its absorbance. Hence, utilizing the equation $y = 0.0353x - 0.0205$,

the concentration of the MO solution can be readily determined. Therefore, for the upcoming MO photocatalytic degradation experiment, an initial concentration of 15 mg/L will be employed.

The UV-Visible absorption spectra of the MO dye solution during photocatalysis, along with the experimental results for the photodegradation efficiency (η), were investigated for various systems: intrinsic self-decomposition of MO, pristine $TiO_2$-NRAs, pure BiOI-NFs, BiOI/Au-NPs, $TiO_2$-NRAs/BiOI-NFs, and $TiO_2$-NRAs/BiOI-NFs/Au-NPs nano-hybrids. The experiments were conducted under UV-Visible lamp irradiation (photon-flux of 77.5 $W/m^2$) for 180 minutes at ambient temperature, as depicted in Figure 11. The photodegradation coefficient, denoted as η, was calculated using the formula: $\eta = (C_0 - C)/C_0 \times 100\%$, where $C_0$ and C represent the initial and final concentrations of MO after radiation exposure. As illustrated in Figure 11, the intrinsic self-photodegradation of MO was negligible, accounting for less than 4% and could be disregarded. Furthermore, the pristine $TiO_2$-NRAs and pure BiOI-NFs specimens exhibited inferior photodegradation performance, approximately 25.1% and 31.1% respectively, under UV-Visible lamp irradiation. This can be attributed to their limited photo-absorption ability in the visible light range and the scarcity of surface-active adsorption sites related with vacancies defects in the separated semiconductors. In contrast, the binary nanoheterojunctions of BiOI-NFs/Au-NPs and $TiO_2$-NRAs/BiOI-NFs demonstrated significantly enhanced photodegradation rates towards MO, approximately 65.6% and 81.2% respectively, surpassing the performance of individual semiconductors. This improvement can be attributed to the combined effect of a broader light absorption range and a step-wise energy band structure inherent in conventional type-II heterostructures. These factors generated a strong driving force for the BEF, facilitating the generation of more energetic carriers involved in the redox reaction. Remarkably, the $TiO_2$-NRAs/BiOI-NFs/Au-NPs composite exhibited the most remarkable photodegradation activity, reaching approximately 96.6% degradation of MO. This can be mainly attributed to the synergistic effect of abundant highly active carriers, a large number of surface vacancies defects, and the aforementioned dominant factors.

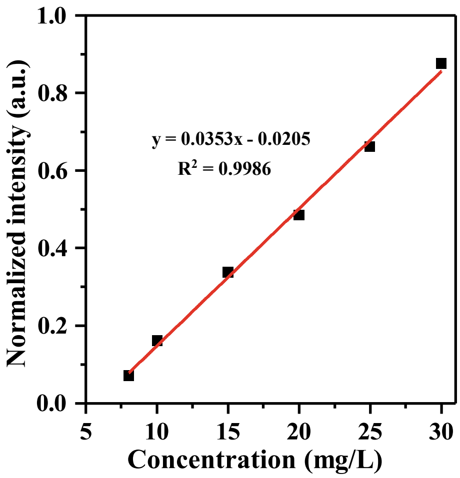

**Figure 10.** Calibration curve for MO at various concentrations.

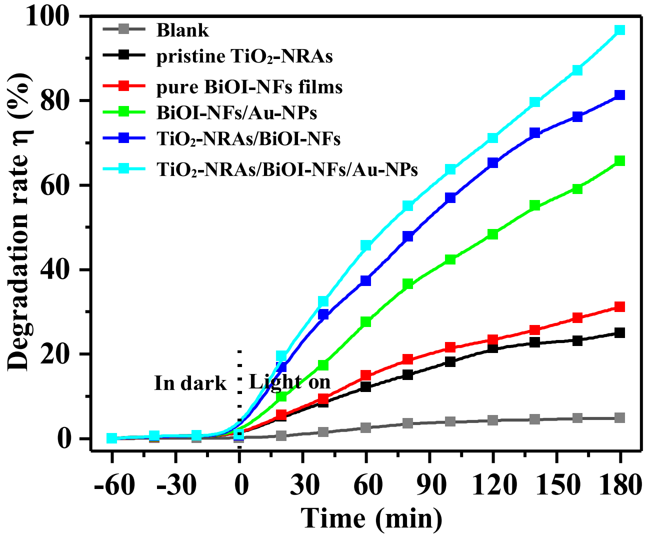

**Figure 11.** Photodegradation rate of MO and as-prepared samples under UV-Visible light irradiation at room temperature for 180 minutes, respectively.

To quantitatively assess the reaction dynamics, we adopted the pseudo-first-order (PFO) kinetic model to describe the photocatalytic behavior of the MO aqueous solution. The model is represented by the equation $\ln(C_0/C_t) = kt$, where k, $C_0$, and $C_t$ correspond to the reaction rate constant, initial concentration, and concentration at time t of MO, respectively. Figure 12 illustrates this model, including the self-degradation reaction of MO. By plotting $\ln(C_0/C_t)$ against time, the rate constant can be determined. All the curves exhibit a peak value for the PFO rate constant, emphasizing the superiority of the ternary $TiO_2$-NRAs/BiOI-NFs/Au-NPs nanohetero-hybrids. This observation suggests that the Z-scheme CT mechanism employed by this particular system promotes efficient charge separation, leading to the highest overall efficiency compared to other heterostructures.

In addition to photodegradation efficiency, recycling usability and stability are crucial factors contributing to the financial feasibility and environmental sustainability of the process. To investigate the potential reusability of the BiOI-related heterostructure nano-hybrids, a series of

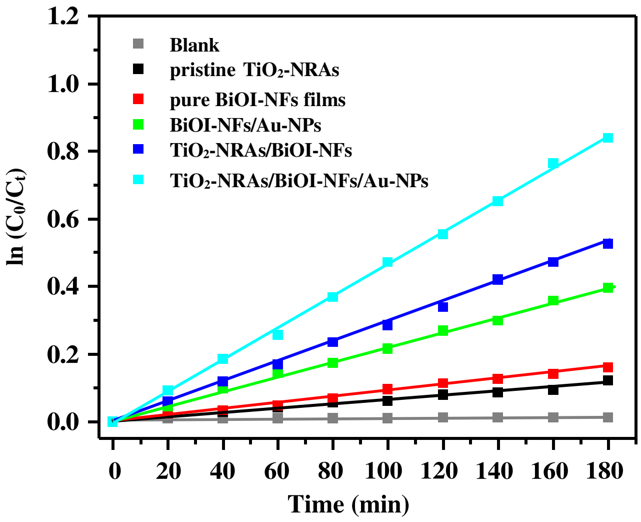

**Figure 12.** Plot of $\ln(C_0/C_t)$ versus irradiation time of MO degradation for MO and as-obtained specimens irradiated by UV-Visible light at room temperature, respectively.

cyclic photocatalytic experiments were conducted. These experiments involved subjecting the specimens to UV-Visible light for six consecutive cycles under identical conditions, as depicted in Figure 13. After each cycle, the specimens were thoroughly washed with deionized water and then dried overnight in an oven before being reused. The findings revealed a slight decline in the photodegradation efficiency of the binary and ternary hetero-nanocomplexes for MO removal. This decline can be expected due to the inevitable weight loss during the collection and washing process. However, even after six consecutive cycles, the deterioration of photodegradation performance for the ternary nanohybrids (approximately 9.6%) was significantly less compared to the binary nanoheterojunctions (approximately 12.5% and 14.3%). This fully demonstrates the high stability of the as-crafted ternary nano-hybrids in comparison to the binary nano-systems. The decoration of ternary heterostructure thin-films with Au-NPs proves to be an excellent strategy for increasing electron density. This is attributed to the Au-NPs serving as donors of hot electrons, which leads to a significant enhancement in durability and robustness properties. This strategy has been shown to improve the overall stability and longevity of the photocatalytic system. (Shi et al., 2023; Rafique et al., 2023) As depicted in Figure 14; the photodegradation activity of TiO$_2$-NRAs/BiOI-NFs/Au-NPs reached approximately 96.6% in the absence of radical scavengers. However, in the presence of methanol and IPA as h$^+$ and ·OH scavenger agents respectively, the values of η were around 65.2% and 63.4% respectively. To create a clearer distinction, high-purity N$_2$ gas was continuously infused throughout the degradation process. This was done to eliminate dissolved O$_2$ and inhibit the generation of $\cdot O_2^-$. Under standard atmospheric conditions and room temperature, when subjected to UV-Visible light for a duration of 180 minutes, the degradation of MO occurred at a rate of approximately 30.6%. Notably, this degradation rate is significantly lower compared to the 96.6% degradation observed under the aforementioned conditions. This degradation process involved the participation of h$^+$, ·OH, and $\cdot O_2^-$ radical groups, with $\cdot O_2^-$ being the primary reactive species, as expected. The efficiency of the reaction was found to be strongly influenced by the quantity of surface-active adsorption sites induced by the presence of vacancies defects.

Table 1 presents a comprehensive comparison of the photodegradation efficiencies for MO organic pollutants by different ternary nanoheterojunction composite materials. Besides the AgI/BiOI/g-C$_3$N$_4$ nanocomposite, which exhibits a removal rate of 90% within 50 minutes, the TiO$_2$-NRAs/BiOI-NFs/Au-NPs ternary nanoheterostructure synthesized via electrodeposition in the present work demonstrates the highest photodegradation efficiency, achieving an outstanding MO removal rate of 96.6% within 180 minutes of photocatalytic treatment.

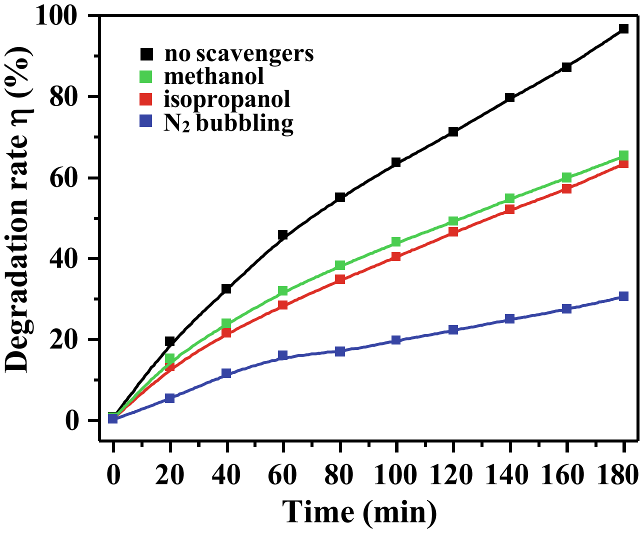

**Figure 14.** Photodegradation efficiency of MO dye for the specimen of TiO$_2$-NRAs/BiOI-NFs/Au-NPs with and without the presence of scavengers irradiated by UV-Visible light, respectively.

This superior performance highlights the excellent cost-effectiveness of the as-prepared TiO$_2$-NRAs/BiOI-NFs/Au-NPs ternary nanoheterostructure compared to other ternary nanoheterojunction systems. Furthermore, it reaffirms the existence of an efficient Z-scheme charge transfer pathway, as well as the synergistic effects of plasmon-induced hot electron injection and abundant V$_o$ defects in the ternary nanosystem, contributing to its exceptional PEC activity.

The photodegradation experiments for the specimens of single MO, pure BiOI-NFs, BiOI/Au-NPs, TiO$_2$-NRAs/BiOI-NFs, and TiO$_2$-NRAs/BiOI-NFs/Au-NPs nano-hybrids were performed irradiated by NIR light for 180 minutes at ambient temperature, as depicted in Fig 15.

15. It can be clearly observed that the intrinsic self-photodegradation of MO was negligible, accounting for less than 3% and could be disregarded. Furthermore, the pristine BiOI-NFs specimens exhibited least photocatalytic performance with photodegradation rate approximately 5.18% under NIR lamp irradiation. This can be mainly attributed to the fact that the energy of the incident infrared photons (ca. 1.59 eV) is smaller than the E$_g$ value of single BiOI-NFs, thereby failing to effectively generate photogenerated charge carriers involved in the PEC reaction. Simultaneously, the TiO$_2$-NRAs/BiOI-NFs binary nanohybrid

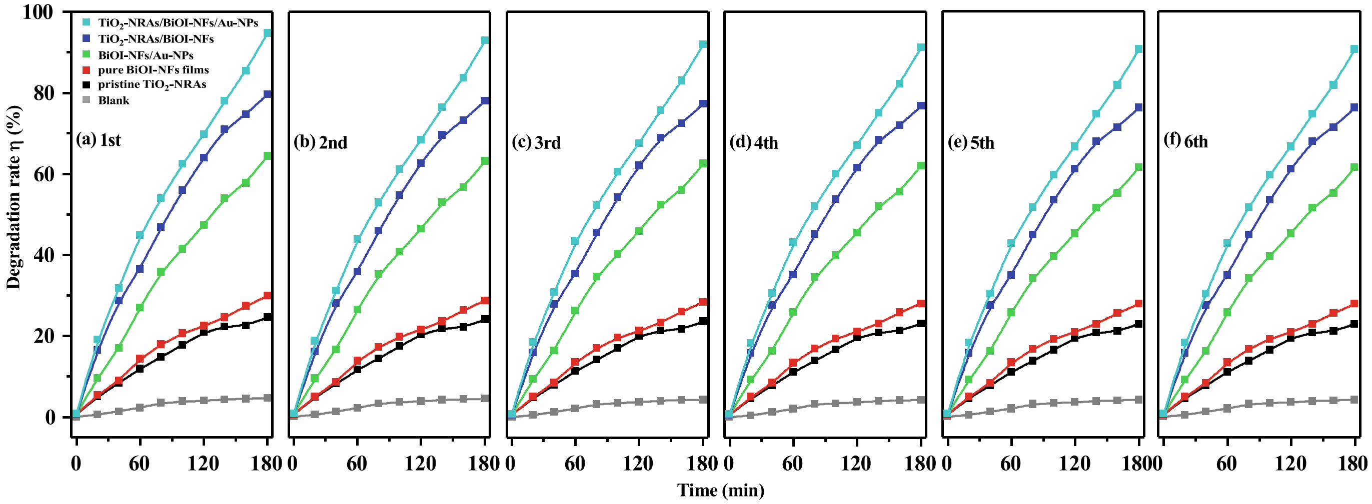

**Figure 13.** Cyclic photodegradation efficiency of the MO and the thus-obtained specimens irradiated by UV-Visible light under the same conditions six times, respectively.

**Table 1**
Comprehensive comparison of the photodegradation efficiencies of MO organic pollutants by different ternary nanoheterojunction composite materials.

| sample | synthesis method | target pollutant | time (min) | Removal rate (%) | reference |
|---|---|---|---|---|---|
| AgBr/BiOI/g-$C_3N_4$ | wet impregnation | MO | 120 | 93.4 | (Li et al., 2022) |
| AgI/BiOI/g-$C_3N_4$ | ultra-sonication | MO | 50 | 90 | (Yuan et al., 2020) |
| BiOBr/BiOCl/PANI | co-precipitation | MO | 240 | 89 | (Berijani and Bahramian, 2021) |
| $TiO_2$/BiOI/CQDs | co-precipitation | MO | 180 | 90 | (Zhao et al., 2017) |
| AgI/BiOI/CNFs | electrospinning | MO | 198 | 92.1 | (Zhang et al., 2019) |
| Au/BiOCl/$BiVO_4$ | chemical reduction | MO | 240 | 67 | (Galvana et al., 2019) |
| Ag/AgI/BiOI | ion-exchange | MO | 180 | 93 | (Cao et al., 2017) |
| $TiO_2$-NRAs/BiOI-NFs/Au-NPs | electro-deposition | MO | 180 | 96.6 | present work |

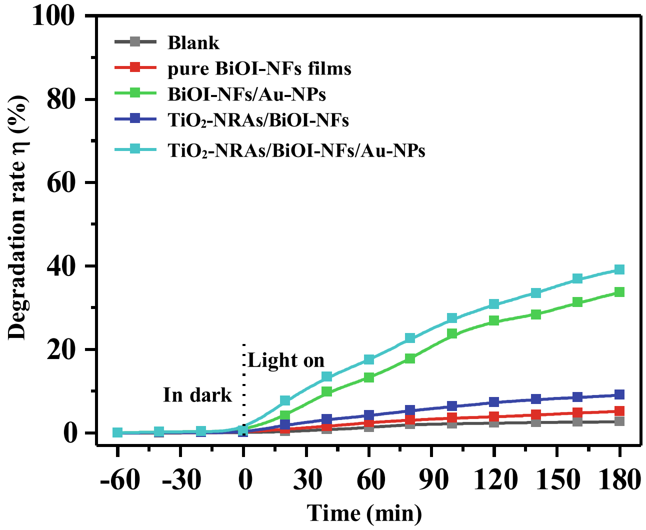

**Figure 15.** Photodegradation rate of MO and as-prepared specimens under near infrared light (NIR) irradiation at room temperature for 180 min, respectively.

exhibited inferior PEC activity, with a photodegradation rate of only 9.02%. This can be mainly attributed to the inability of the incident photon energy to effectively excite the $TiO_2$-NRAs/BiOI-NFs binary nanohybrid to generate photogenerated free charge carriers. Moreover, compared to the single BiOI-NFs, the $TiO_2$-NRAs/BiOI-NFs binary nanoheterojunction possesses more vacancies defects, enabling the adsorption of active sites. Consequently, the photodegradation rate of the binary nanoheterojunction is higher than that of the single semiconductor. In contrast, the binary nanoheterojunctions of BiOI-NFs/Au-NPs demonstrated significantly enhanced photodegradation rates towards MO (ca. 33.7%) under NIR light irradiation, surpassing the PEC performance of $TiO_2$-NRAs/BiOI-NFs. This can be mainly ascribed to the generation of plasmon-induced hot electron in Au-NPs irradiated by NIR light, and then injected into the adjacent BiOI-NFs driven by the BEF, facilitating the generation of more energetic carriers involved in the redox reaction. Remarkably, the $TiO_2$-NRAs/BiOI-NFs/Au-NPs ternary nanocomposites exhibited the most remarkable photodegradation activity, reaching approximately 39.1% degradation of MO under NIR light irradiation. This can be mainly attributed to the synergistic effects of the Z-scheme CT mechanism, abundant highly active carriers induced by plasmon-induced hot electron injection, and a large number of surface active sites caused by vacancies defects.

Figure 16 shows a plot of $\ln(C_0/C_t)$ versus irradiation time for the photocatalytic degradation of MO under NIR light irradiation at room temperature. The plot compares the degradation kinetics of MO alone (self-degradation) and the as-obtained photocatalyst specimens, including pure BiOI-NFs, binary BiOI-NFs/Au-NPs, $TiO_2$-NRAs/BiOI-NFs nanohybrids, and $TiO_2$-NRAs/BiOI-NFs/Au-NPs ternary nanoheterojunctions. The PFO kinetic model, represented by the equation $\ln(C_0/C_t) = kt$, is used to quantitatively assess the reaction dynamics. In this model, k is the reaction rate constant, $C_0$ is the initial MO concentration, and $C_t$ is the MO concentration at time t, as stated above. The plot reveals that all the photocatalyst specimens exhibit higher degradation rates compared to the self-degradation of MO. Furthermore, the ternary $TiO_2$-NRAs/BiOI-NFs/Au-NPs nanoheterojunctions demonstrate the highest PFO rate constant, indicating superior PEC performance. This observation suggests that the Z-scheme CT mechanism employed by this ternary system promotes efficient plasmon-induced hot electron transfer, leading to the highest overall photocatalytic efficiency among the examined heterostructures.

Figure 17 illustrates the cyclic photodegradation efficiency of MO and the obtained specimens, including pristine BiOI-NFs, BiOI-NFs/Au-NPs, $TiO_2$-NRAs/BiOI-NFs nanohybrids, and $TiO_2$-NRAs/BiOI-NFs/Au-NPs ternary nanoheterojunctions, under NIR light irradiation for six consecutive cycles under the same conditions. After each cycle, the photocatalyst specimens were thoroughly washed with deionized water and dried overnight in an oven before being reused for the next cycle. The results reveal a slight decline in the photodegradation efficiency of the binary and ternary hetero-nanocomplexes for MO removal after multiple cycles. This decline can be expected due to the inevitable weight loss during the collection and washing process.

However, the ternary $TiO_2$-NRAs/BiOI-NFs/Au-NPs nanoheterojunctions exhibited significantly higher stability and durability compared to the binary BiOI-NFs/Au-NPs and $TiO_2$-NRAs/BiOI-NFs nanoheterojunctions. Even after six consecutive cycles, the deterioration

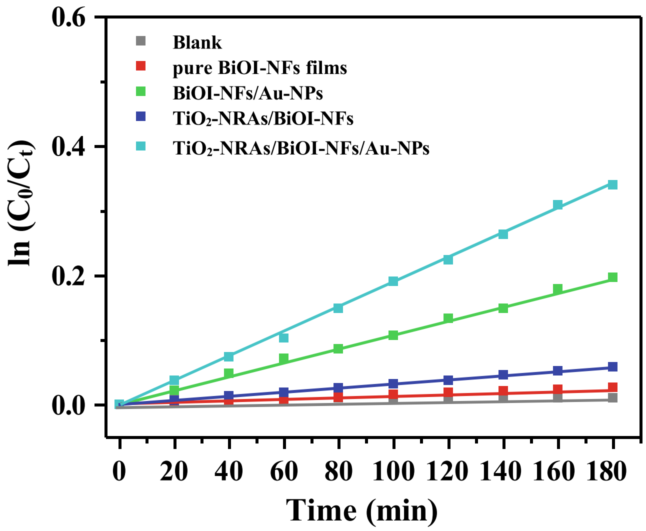

**Figure 16.** Plot of $\ln(C_0/C_t)$ versus irradiation time of MO degradation for MO and as-obtained specimens irradiated by NIR light at room temperature, respectively.

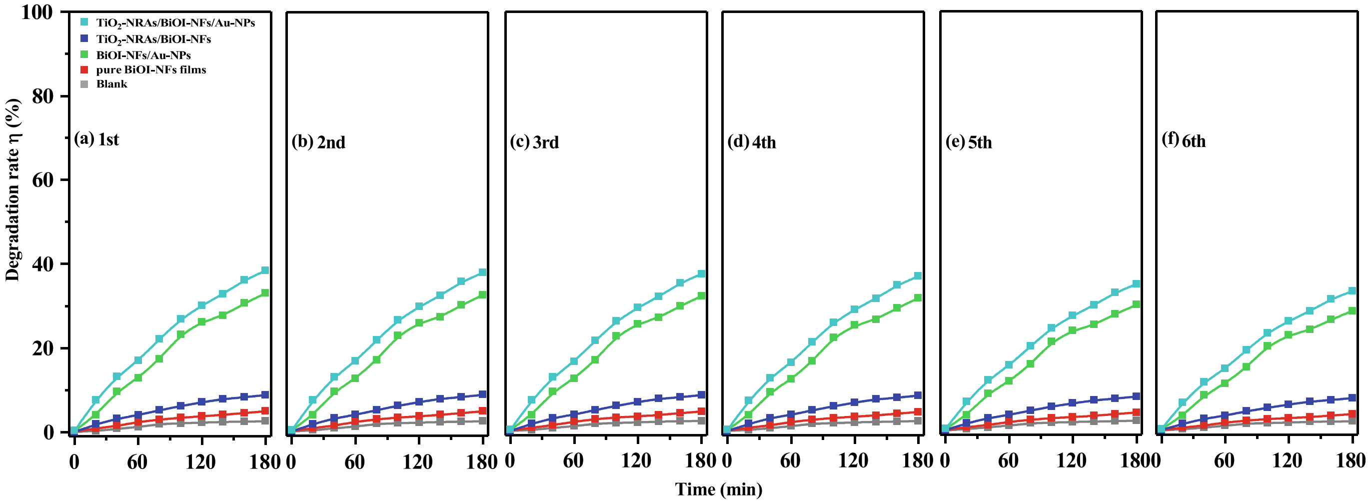

**Figure 17.** Cyclic photodegradation efficiency of the MO and the thus-obtained specimens irradiated by NIR light under the same conditions six times, respectively.

of photodegradation performance for the ternary nanohybrids (approximately 8.9%) was considerably less compared to the binary nanoheterojunctions (approximately 11.6% and 13.3%). This superior stability of the ternary nanohybrids is attributed to the decoration of Au-NPs in the heterostructure thin-films. The Au-NPs serve as donors of hot electrons irradiated by NIR light, leading to an increased electron density and significantly enhancing the durability and robustness properties of the ternary photocatalytic system.

## 4. Conclusion

In conclusion, we have successfully achieved the synthesis of plasmon M-S junction, binary type-II heterojunction, and Z-scheme heterostructured nano-hybrids through an accessible synthesis method. The constructed Au-NPs mediated Z-scheme $TiO_2$-NRAs/BiOI-NFs/Au-NPs ternary electrode exhibit impressive enhancements in photodegradation performance when compared to BiOI-NFs/Au-NPs and $TiO_2$-NRAs/BiOI-NFs binary nanoheterostructures under simulated sunlight irradiation. This result was mainly ascribed to the synergistic effects of the most effective CT channel and the strongest redox capability in such Z-scheme junction. Our proposition finds support in the characterization of NTRT-PL spectra, offering a plausible mechanism for the Z-scheme CT dynamics process occurred at the heterojunction interfaces, which revealed a significant increase in the concentrations of energetic electrons induced by plasmon resonance and an improvement in the amount of active adsorption sites associating with $V_o$ defects. This work endeavors to provide a novel perspective on the fabrication of high-performance photocatalysts by leveraging the unique Z-scheme CT mechanism facilitated by the ternary heterostructure of $TiO_2$-NRAs/BiOI-NFs/Au-NPs.

## CRediT authorship contribution statement

**Zhufeng Shao:** Conceptualization, Funding acquisition, Writing – original draft. **Yonglong Zhang:** Data curation, Investigation, Methodology. **Xiujuan Yang:** Formal analysis, Methodology. **Guoyang Yu:** Investigation. **Yunfei Song:** Investigation. **Min Zhong:** Writing – review & editing. **Xiaoming Xiu:** Writing – review & editing.

## Declaration of competing interest

The authors declare that they have no known competing financial interests or personal relationships that could have appeared to influence the work reported in this paper.

## Acknowledgements

This work was financially supported by the general project of Liaoning provincial department of education (Project No. LJKMZ20221494)

## Appendix A. Supplementary data

Supplementary data to this article can be found online at https://doi.org/10.1016/j.arabjc.2024.105765.

## References

An, R., Zhao, Y., Bai, H., Wang, L., Li, C., 2022. Decoration of Au NPs on hollow structured BiOBr with surface oxygen vacancies for enhanced visible light photocatalytic $H_2O_2$ evolution. J. Solid State Chem. 306, 122722.

Berijani, M.Y., Bahramian, B., 2021. Preparation and measurement of properties of BiOBr/BiOCl/PANI ternary nanocomposite for highly efficient visible light photocatalytic applications. Res. Chem. Intermed. 47, 2311–2330.

Bopape, D.A., Tetana, Z.N., Mabuba, N., Motaung, D.E., Hintsho-Mbita, N.C., 2023. Biosynthesis of $TiO_2$ nanoparticles using Commelina benghanlensis for the photodegradation of methylene blue dye and antibiotics: Effect of plant concentration. Results in Chemistry 5, 100825.

Cao, J., Zhao, Y., Lin, H., Xu, B., Chen, S., 2017. Facile synthesis of novel Ag/AgI/BiOI composites with highly enhanced visible light photocatalytic performances. J. Solid State Chem. 206, 38–44.

Chen, J., He, J., Yin, Z., Wang, T., Liu, S., Cao, S., 2023. One-pot synthesis of porous $TiO_2$/BiOI adsorbent with high removal efficiency and excellent recyclability towards tetracyclines. Ceram. Int. 49, 22139–22148.

Chen, L., Li, C., Zhao, Y., Wu, J., Li, X., Qiao, Z., He, P., Qi, X., Liu, Z., Wei, G., 2021. Constructing 3D $Bi/Bi_4O_5I_2$ microspheres with rich oxygen vacancies by one-pot solvothermal method for enhancing photocatalytic activity on mercury removal. Chem. Eng. J. 425, 131599.

Chen, X., Peng, X., Jiang, L., Yuan, X., Fei, J., Zhang, W., 2022. Photocatalytic removal of antibiotics by MOF-derived Ti3+- and oxygen vacancy-doped anatase/rutile TiO2 distributed in a carbon matrix. Chem. Eng. J. 427, 130945.

Cui, X., Zhang, X., Yang, Z., Xiao, M., Ren, J., Xiao, X., Wang, Y., 2022. The rod-like $CeO_2$ supported by the low-loading Au nanoparticles for the efficient catalytic oxidation of CO at room temperature. Int. J. Hydrogen Energy 47, 11813–11826.

Fu, X., Li, G.G., Villarreal, E., Wang, H., 2019. Hot carriers in action: multimodal photocatalysis on Au@$SnO_2$ core–shell nanoparticles. Nanoscale 11, 7324–7334.

Fu, Y., Yu, Q., Zhang, Q., Zhang, X., Du, C., Chen, J., 2021. A photocurrent-polarity-switching biosensor for highly selective assay of mucin 1 based on target-induced hemin transfer from $ZrO_2$ hollow spheres to G-quadruplex nanowires. Biosens. Bioelectron. 192, 113547.

Fujishima, A., Honda, K., 1972. Electrochemical photolysis of water at a semiconductor electrode. Nature 238, 37–38.

Galvana, M.G., Robledoa, P.Z., Arenasb, J.V., Ibarrac, I.R., Ostosd, C., Perale, J., Pereza, U.M.G., 2019. In situ synthesis of Au-decorated BiOCl/$BiVO_4$ hybrid ternary system with enhanced visible-light photocatalytic behavior. Appl. Surf. Sci. 487, 743–754.

Guan, X., Zhang, X., Zhang, C., Li, R., Liu, J., Wang, Y., Wang, Y., Fan, C., Li, Z., 2022. In Situ hydrothermal synthesis of metallic Bi self-deposited $Bi_2SiO_5$ with enhanced photocatalytic $CO_2$ reduction performance. Solar RRL 6, 2200346.

Güntner, A.T., Schenk, F.M., 2023. Environmental formaldehyde sensing at room temperature by smartphone-assisted and wearable plasmonic nanohybrids. Nanoscale 15, 3967–3977.

Hoseini, A., Yarmand, B., 2023. Enhanced photocatalytic performance and photocorrosion stability of PEO-immobilized $TiO_2$ photocatalyst using rGO/$Fe_2O_3$ sensitizers. Surf. Interfaces 42, 103424.

Hu, Q., Dong, J., Chen, Y., Yi, J., Xia, J., Yin, S., Li, H., 2022. In-situ construction of bifunctional MIL-125(Ti)/BiOI reactive adsorbent/photocatalyst with enhanced removal efficiency of organic contaminants. Appl. Surf. Sci. 583, 152423.

Huang, Y.S., Gierschner, J., Schmidtke, J.P., Friend, R.H., Beljonne, D., 2011. Tuning interchain and intrachain interactions in polyfluorene copolymers. Phys. Rev. B 84, 205311.

Huang, Z., Li, Z., Zhang, X., Zhang, Z., Chen, J., 2023. (001) Facets optimized surface oxygen vacancies in TiO2 films to enhance photocatalytic antibacterial and hydrophilic properties. Appl. Surf. Sci. 616, 156571.

Ji, J., Zhang, C., Yang, X., Kong, F., Wu, C., Duan, H., Yang, D., 2023. Pt-stabilized electron-rich Ir structures for low temperature methane combustion with enhanced sulfur-resistance. Chem. Eng. J. 143044.

Jin, J., Liu, Y., Zhao, X., Liu, H., Deng, S., Shen, Q., Hou, Y., Qi, H., Xing, X., Jiao, L., Chen, J., 2023. Annealing in argon universally upgrades the Na-storage performance of Mn-based layered oxide cathodes by creating bulk oxygen vacancies. Angew. Chem. Int. Ed. 62, e202219230.

Ju, P., Zhang, Y., Hao, L., Cao, J., Zhai, X., Dou, K., Jiang, F., Sun, C., 2023. 1D $Bi_2S_3$ nanorods modified 2D BiOI nanoplates for highly efficient photocatalytic activity: Pivotal roles of oxygen vacancies and Z-scheme heterojunction. J. Mater. Sci. Technol. 142, 45–59.

Kaur, M., Ahmad Mir, R., Chauhan, I., Singh, K., Krishnan, U., Kumar, M., Devi, P., Pandey, O.P., Kumar, A., 2021. Defect states induced luminescence and electrochemical studies of boron carbon nitride nanosheets. Appl. Surf. Sci. 559, 149982.

Krishna, D.N.G., Philip, J., 2022. Review on surface-characterization applications of X-ray photoelectron spectroscopy (XPS): Recent developments and challenges. Applied Surface Science Advances 12, 100332.

Kumara, K., Kindalkar, V.S., Jyothi Serrao, F., T. Chandra Shekhara Shetty, P.S. Patil, S. M. Dharmaprakash,, 2022. Enhanced nonlinear optical absorption in defect enriched graphene oxide and reduced graphene oxide using continuous wave laser z-scan technique 55, 186–193.

Li, X., Ai, M., Zhang, X., Zou, J.J., Pan, L., 2022. Dual co-catalysts decorated Zn-$WO_3$ nanorod arrays with highly efficient photoelectrocatalytic performance. Int. J. Hydrogen Energy 47, 13641–13653.

Li, J., Fang, S., Xu, L., Wang, A., Zou, K., Di, A., Li, F., Deng, W., Zou, G., Hou, H., Ji, X., 2022. Electrochemical Zintl Cluster $Bi_2^{2-}$ induced chemically bonded bismuth/graphene oxide composite for sodium-ion batteries. Electrochim. Acta 413, 140174.

Li, Y., Li, Z., Xia, Y., Gao, L., 2022. AgBr/BiOI/g-C3N4 photocatalyst with enhanced photocatalytic activity under visible-light irradiation via the formation of double Z-Type heterojunction with the synergistic effect of metal Ag. Ind. Eng. Chem. Res. 61, 12918–12930.

Li, Y., Zhang, H., Qian, W., Xia, Y., Li, D., Guo, Z., 2023. Construction of S-scheme heterostructured $TiO_2$/g-$C_3N_4$ composite microspheres with sunlight-driven photocatalytic activity. MaterialsToday Communications 36, 106431.

Liao, X., Li, T.T., Ren, H.T., Zhang, X., Shen, B., Lin, J.H., Lou, C.W., 2022. Construction of BiOI/$TiO_2$ flexible and hierarchical S-scheme heterojunction nanofibers membranes for visible-light-driven photocatalytic pollutants degradation. Sci. Total Environ. 806, 150698.

Liu, X., Chen, J., Yang, L., Yun, S., Que, M., Zheng, H., Zhao, Y., Yang, T., Liu, Z., 2022. 2D/2D g-C3N4/TiO2 with exposed (001) facets Z-Scheme composites accelerating separation of interfacial charge and visible photocatalytic degradation of Rhodamine B. J. Phys. Chem. Solid 160, 110339.

Liu, Y., Wang, J., Yang, P., Matras-Postolek, K., 2015. Self-modification of TiO2 one-dimensional nano-materials by Ti3+ and oxygen vacancy using Ti2O3 as precursor. RSC Adv. 5, 61657–61663.

Lu, Y., Deng, H., Pan, T., Zhang, C., He, H., 2023. Thermal annealing induced surface oxygen vacancy clusters in α-$MnO_2$ nanowires for catalytic ozonation of VOCs at ambient temperature. ACS Appl. Mater. Interfaces 15, 9362–9372.

Mao, S., Sun, B., Ke, C., Qin, J., Yang, Y., Guo, T., Wu, Y.A., Shao, J., Zhao, Y., 2023. Evolution between CRS and NRS behaviors in $MnO_2$@$TiO_2$ nanocomposite based memristor for multi-factors-regulated memory applications. Nano Energy 107, 108117.

Mohamed, H.S.H., Rabia, M., Zhou, X.G., Qin, X.S., Khabiri, G., Shaban, M., Younus, H. A., Taha, S., Hu, Z.Y., Liu, J., Li, Y., Su, B.L., 2021. Phase-junction Ag/$TiO_2$ nanocomposite as photocathode for $H_2$ generation. J. Mater. Sci. Technol. 83, 179–187.

Prusty, D., Mansingh, S., Acharya, L., Paramanik, L., Parida, K.M., 2022. Robust direct Z-scheme exciton transfer dynamics by architecting 3D BiOI MF-supported non-stoichiometric $Cu_{0.75}In_{0.25}S$ NC nanocomposite for co-catalyst-free photocatalytic hydrogen evolution, RSC. Advances 12, 1265–1277.

Qiao, J., Wang, Y., Dong, S., Liang, Q., Shao, S., 2023. Au nanoparticles-decorated BiOI nanosheet arrays for cathodic photoelectrochemical dopamine sensors. ACS Applied Nano Materials 6, 5664–5674.

Qu, W., Chen, C., Tang, Z., Xia, D., Ma, D., Huang, Y., Lian, Q., He, C., Shu, D., Han, B., 2022. Electron-rich/poor reaction sites enable ultrafast confining Fenton-like processes in facet-engineered BiOI membranes for water purification. Appl Catal B 304, 120970.

Rafique, N., Asif, A.H., Hirani, R.A.K., Wu, H., Shi, L., Zhang, S., Wang, S., Yin, Y., Wang, S., Sun, H., 2023. Versatile heterojunction of gold nanoparticles modified phosphorus doped carbon nitride for enhanced photo-electrocatalytic sensing and degradation of 4-chlorophenol. J. Colloid Interface Sci. 632, 117–128.

Shan, L., Fang, Z., Ding, G., Shi, Z., Dong, L., Li, D., Wu, H., Li, X., Suriyaprakash, J., Zhou, Y., Xiao, Y., 2024. Electron confinement promoted the electric double layer effect of BiOI/β-$Bi_2O_3$ in photocatalytic water splitting. J. Colloid Interface Sci. 653, 94–107.

Shao, Z., Tian, Z., Pang, J., Feng, G., Guo, B., Zeng, C., Yang, Y., Liu, S., Wang, Q., 2014. Optically modulated charge transfer in $TiO_2$-Au nano-complexes. Mater. Res. Express 1, 045033.

Shao, Z., Liu, W., Zhang, Y., Yang, X., Zhong, M., 2021. Insights on interfacial charge transfer across $MoS_2$/$TiO_2$-NTAs nanoheterostructures for enhanced photodegradation and biosensing&gas-sensing performance. J. Mol. Struct. 1244, 131240.

Shao, Z., Cheng, J., Zhang, Y., Peng, Y., Shi, L., Zhong, M., 2022. Comprehension of the synergistic effect between m&t-$BiVO_4$/$TiO_2$-NTAs nano-heterostructures and oxygen vacancy for elevated charge transfer and enhanced photoelectrochemical performances. Nanomaterials 12, 4042.

Shao, Z., Zhang, Y., Cheng, J., Shi, L., Yang, X., Xiu, X., 2023. Comparing defect-assisted interfacial charge transfer in CdS/PSA and CdS/$TiO_2$-NTAs nanoheterojunctions for enhanced photodegradation and biosensing. Applied Surface Science Advances 18, 100464.

Shi, Q., Zhang, X., Li, Z., Raza, A., Li, G., 2023. Plasmonic Au nanoparticle of a Au/$TiO_2$–$C_3N_4$ heterojunction boosts up photooxidation of benzyl alcohol using LED light. ACS Appl. Mater. Interfaces 15, 30161–30169.

Shilpa, G., M.K. P, P.R. Deepthi, R. Balan, A. Sukhdev, P. Bhaskar, K. Kumar D,, 2023. Enhanced photocatalytic activity of orientationally grown CQD/$TiO_2$ thin film on FTO substrate. Ceram. Int. 49, 19083–19090.

Silva, I.O., Ladchumananandasivam, R., Nascimento, J.H.O., Silva, K.K.O.S., Oliveira, F. R., Souto, A.P., Felgueiras, H.P., Zille, A., 2019. Multifunctional chitosan/gold nanoparticles coatings for biomedical textiles. Nanomaterials 9, 1064.

Sun, J., Li, X., Zhao, Q., Liu, B., 2021. Ultrathin nanoflake-assembled hierarchical BiOBr microflower with highly exposed 001 facets for efficient photocatalytic degradation of gaseous ortho-dichlorobenzene. Appl Catal B 281, 119478.

Sun, L., Yu, X., Tang, L., Wang, W., Liu, Q., 2023. Hollow dodecahedron $K_3PW_{12}O_{40}$/CdS core-shell S-scheme heterojunction for photocatalytic synergistic $H_2$ evolution and benzyl alcohol oxidation. Chin. J. Catal. 52, 164–175.

Wang, G., Cai, Y., Jiang, H., Liu, F., Yi, K., Wang, D., 2023. Combinatorial tuning of work function and optical properties in CuZnSe thin films for efficient bifacial CdTe solar cells. Sol. Energy Mater. Sol. Cells 255, 112312.

Wang, Z., Cheng, B., Zhang, L., Yu, J., Li, Y., Wageh, S., Al-Ghamdi, A.A., 2022. S-Scheme 2D/2D $Bi_2MoO_6$/BiOI van der Waals heterojunction for $CO_2$ photoreduction. Chin. J. Catal. 43, 1657–1666.

Wang, H., Cheng, X., Kups, T., Sun, S., Chen, G., Wang, D., Schaaf, P., 2022. Hydrogenated $TiO_2$ nanoparticles loaded with Au nanoclusters demonstrating largely enhanced performance for electrochemical reduction of nitrogen to ammonia. Energ. Technol. 10, 2200085.

Wang, Q., Guo, L., Gao, W., Li, S., Hao, L., Wang, Z., Wang, C., Wu, Q., 2022. Facile synthesis of BiOI/MXene heterostructure as a superior photoelectrochemical sensor for sensitive detection of glucose. Anal. Chim. Acta 1233, 340511.

Wang, W., Mei, S., Jiang, H., Wang, L., Tang, H., Liu, Q., 2023. Recent advances in $TiO_2$-based S-scheme heterojunction photocatalysts. Chin. J. Catal. 55, 137–158.

Wang, Q., Qian, X., Xu, H., He, G., Chen, H., 2023. Enriched surface oxygen vacancies of Bi2WO6/NH2-MIL-68(In) Z-scheme heterojunction with boosted visible-light photocatalytic degradation for levofloxacin: Performance, degradation pathway and mechanism insight. Sep. Purif. Technol. 306, 122577.

Wang, L., Yang, T., Peng, L., Zhang, Q., She, X., Tang, H., Liu, Q., 2022. Dual transfer channels of photo-carriers in 2D/2D/2D sandwich-like $ZnIn_2S_4$/g-$C_3N_4$/$Ti_3C_2$ MXene S-scheme/Schottky heterojunction for boosting photocatalytic $H_2$ evolution. Chin. J. Catal. 43, 2720–2731.

Wang, X., Zhu, J., Fu, X., Xu, J., Yu, X., Zhu, Y., Zhang, Y., Zhu, M., 2022. Boosted visible-light photocatalytic performance of Au/BiOCl/BiOI by high-speed spatial electron transfer channel. J. Alloy. Compd. 890, 161736.

Wu, M., Jing, T., Tian, J., Qi, H., Shi, D., Zhao, C., Chen, T., Zhao, Z., Zhang, P., Guo, Z., 2022. Synergistic effect of silver plasmon resonance and p-n heterojunction enhanced photoelectrochemical aptasensing platform for detecting chloramphenicol. Advanced Composites and Hybrid Materials 5, 2247–2259.

Wu, Q., Zhang, G., Wang, Y., Jiao, Y., Ma, Y., Zheng, Y., 2023. Seeded growth of gold-based nanoscale homojunctions via controlled etching regrowth and their applications for methanol oxidation reaction. CrstEngComm 25, 660–670.

Xia, C., Lu, R., Han, Q., 2022. Synthesis of $Bi_4O_5I_2$/$Bi_5O_7I$ heterojunction at weak acidic solution with preferentially growing facets and high photocatalytic activity. Opt. Mater. 134, 113184.

Xin, Y., Wang, Z., Yao, H., Liu, W., Miao, Y., Zhang, Z., Wu, D., 2023. Au-mediated Z-scheme $TiO_2$-Au-BiOI photoelectrode for sensitive and selective photoelectrochemical detection of L-cysteine. Sens. Actuators B 393, 134285.

Xu, H.Y., Dai, L.Y., Zhang, L., 2022. Anchoring $Fe_3O_4$ nanoparticles onto flower-like BiOI to fabricate p-n junction for boosting visible-light-driven photocatalytic peroxydisulfate activation. Mater. Lett. 324, 132682.

Yamamura, K., Zhu, L., Irvine, C.P., Scott, J.A., Singh, M., Jallandhra, A., Bansal, V., Phillips, M.R., Ton-That, C., 2022. Defect compensation in nitrogen-doped β-$Ga_2O_3$ nanowires: implications for bipolar nanoscale devices. ACS Applied Nano Materials 5, 12087–12094.

Yang, Z., Zhen, Y., Feng, Y., Jiang, X., Qin, Z., Yang, W., Qie, Y., 2023. Polyacrylonitrile@$TiO_2$ nanofibrous membrane decorated by MOF for efficient filtration and green degradation of PM2.5. J. Colloid Interface Sci. 635, 598–610.

Yin, J., Chen, X., Li, G., Liu, D., Li, C., Li, R., Xie, B., Bitter, J.H., Zhang, J., 2023. Construction of charge transfer chain in $Bi_{12}TiO_{20}$-$Bi_4Ti_3O_{12}$/α-$Bi_2O_3$ composites to accelerate photogenerated charge separation. Nano Res. 16, 3730–3740.

Yosefi, L., Haghighi, M., 2018. Fabrication of nanostructured flowerlike p-BiOI/p-NiO heterostructure and its efficient photocatalytic performance in water treatment under visible-light irradiation. Appl Catal B 220, 367–378.

Yu, X., Qiu, H., Wang, Z., Wang, B., Meng, Q., Sun, S., Tang, Y., Zhao, K., 2021. Constructing the Z-scheme $TiO_2$/Au/BiOI nanocomposite for enhanced photocatalytic nitrogen fixation. Appl. Surf. Sci. 556, 149785.

Yuan, D., Huang, L., Li, Y., Wang, H., Xu, X., Wang, C., Yang, L., 2020. A novel AgI/BiOI/pg-$C_3N_4$ composite with enhanced photocatalytic activity for removing methylene orange, tetracycline and E. coli. Dyes Pigm. 177, 108253.

Zhang, Q., Bai, J., Li, G., Li, C., 2019. Synthesis and enhanced photocatalytic activity of AgI-BiOI/CNFs for tetracycline hydrochloride degradation under visible light irradiation. J. Solid State Chem. 270, 129–134.

Zhang, C., Chen, W., Hu, D., Xie, H., Song, Y., Luo, B., Fang, Y., Gao, W., Zhong, Z., 2022. Design and in-situ construct BiOI/Bi/$TiO_2$ photocatalysts with metal-mediated heterostructures employing oxygen vacancies in $TiO_2$ nanosheets, Green. Energy Environ. 7, 680–690.

Zhang, B., Wang, D., Jiao, S., Xu, Z., Liu, Y., Zhao, C., Pan, J., Liu, D., Liu, G., Jiang, B., Li, Y., Zhao, L., Wang, J., 2022. $TiO_{2\text{-}X}$ mesoporous nanospheres/BiOI nanosheets S-scheme heterostructure for high efficiency, stable and unbiased photocatalytic hydrogen production. Chem. Eng. J. 446, 137138.

Zhang, Z., Wu, T., Zhou, H., Jiang, C., Wang, Y., 2021. 3D flower-shaped BiOI encapsulated in molecularly imprinted polymer for hypersensitivity to norfloxacin. Microchem. J. 164, 106017.

Zhang, Q., Xu, J., Li, M., Chen, J., Xu, J., Zheng, Q., Shi, S., Kong, L., Zhang, X., Li, L., 2022. High-performance self-powered ultraviolet photodetector based on BiOCl/$TiO_2$ heterojunctions: Carrier engineering of $TiO_2$. Appl. Surf. Sci. 592, 153350.

Zhang, X., Yang, Z., Zhou, J., Lu, W., Yang, L., 2023. In situ transformation of $TiO_2$ hierarchical nanostructures toward efficient photoelectrochemical water splitting. Ceram. Int. 49, 12061–12068.

Zhao, Y., Fan, X., Zheng, H., Liu, E., Fan, J., Wang, X., 2024. $Bi_2WO_6$/$AgInS_2$ S-scheme heterojunction: Efficient photodegradation of organic pollutant and toxicity evaluation. J. Mater. Sci. Technol. 170, 200–211.

Zhao, C., Liang, Y., Li, W., Tian, Y., Chen, X., Yin, D., Zhang, Q., 2017. BiOBr/BiOCl/carbon quantum dot microspheres with superior visible light-driven photocatalysis, Royal Society of. Chemistry 7, 52614–52620.

Zhao, J., Liu, L., Zhang, Y., Feng, Z., Zhao, F., Wang, W., 2021. Light-responsive color switching of self-doped $TiO_{2-x}$/$WO_3$·0.33$H_2O$ hetero-nanoparticles for highly efficient rewritable paper. Nano Res. 14, 165–171.

Zhou, L., Xie, M., Su, H., Chen, R., Pang, Y., Lou, H., Yang, D., Qiu, X., 2023. In situ oxidation of ethylene glycol coupled with $Bi_2O_3$ epitaxial growth to prepare $Bi_2O_3$/BiOCOOH heterojunctions with oxygen vacancies for efficient photocatalytic lignin degradation. Colloids Surf A Physicochem Eng Asp 664, 131134.

Zhu, B., Hong, X., Tang, L., Liu, Q., Tang, H., 2022. Enhanced photocatalytic CO2 reduction over 2D/1D BiOBr 0.5Cl0.5/WO3 S-scheme heterostructure. Acta Phys. Sin. 38, 2111008.